

# The 30 October 2020 Samos (Eastern Aegean Sea) Earthquake: effects of source rupture, path and local-site conditions on the observed and simulated ground motions

**Aybige Akinci**

Istituto Nazionale di Geofisica e Vulcanologia

**Daniele Cheloni**

Istituto Nazionale di Geofisica e Vulcanologia

**AHMET ANIL DINDAR** (✉ [adindar@gtu.edu.tr](mailto:adindar@gtu.edu.tr))

Gebze Technical University <https://orcid.org/0000-0003-3168-8322>

---

## Research Article

**Keywords:** Earthquake source observations, Satellite geodesy, Ground motions simulations, Site effects, Building damage distribution, Eastern Aegean Sea earthquake

**Posted Date:** February 12th, 2021

**DOI:** <https://doi.org/10.21203/rs.3.rs-215817/v1>

**License:**   This work is licensed under a Creative Commons Attribution 4.0 International License. [Read Full License](#)

---

# Abstract

On 30 October 2020 a  $M_W$  7.0 earthquake occurred in the eastern Aegean Sea, between the Greek island of Samos and Turkey's Aegean coast, causing considerable seismic damage and deaths, especially in the Turkish city of Izmir, approximately 70 km from the epicenter. In this study, we provide a detailed description of the Samos earthquake, starting from the fault rupture to the ground motion characteristics. We first use Interferometric Synthetic Aperture Radar (InSAR) and Global Positioning System (GPS) data to constrain the source mechanisms. Then, we utilize this information to analyze the ground motion characteristics of the mainshock in terms of peak ground acceleration (PGA), peak ground velocity (PGV), and spectral pseudo-accelerations. Modelling of geodetic data shows that the Samos earthquake ruptured a NNE-dipping normal fault located offshore north of Samos, with up to 2.5-3 m of slip and an estimated geodetic moment of  $3.3 \times 10^{19}$  Nm ( $M_W$  7.0). Although low PGA were induced by the earthquake, the ground shaking was strongly amplified in Izmir throughout the alluvial sediments. Structural damage observed in Izmir reveals the potential of seismic risk due to the local site effects. To better understand the earthquake characteristics, we generated and compared stochastic strong ground motions with the observed ground motion parameters as well as the ground motion prediction equations (GMPEs), exploring also the efficacy of the region-specific parameters which may be improved to better predict the expected ground shaking from future large earthquakes in the region.

## 1 Introduction

The 30 October 2020  $M_W$  7.0 Samos (eastern Aegean Sea) earthquake is the largest event to have occurred in the eastern Aegean region. The last significant event in this area was 11 August 1904, when a  $M$  6.8 earthquake struck the south coast of Samos, and caused significant structural damage on Samos and western Anatolia (Turkey). The 30 October 2020 earthquake produced widespread effects including a tsunami, loss of life and severe damage in the epicentral area: in particular, more than 100 people died due to building collapses in the metropolitan area of Izmir (Turkey), and two victims were found in east Samos (Cetin et al. 2020). The earthquake magnitude and epicenter is provided by the various national and international institutes, with rather similar magnitude scales ranging from  $M_W$  6.9 to 7.0. The epicenter was located offshore in the eastern Aegean Sea, between the Greek island of Samos and Turkey's Karaburun peninsula, roughly equidistant from each coast (Fig. 1). The normal faulting mechanism of the mainshock agrees with the almost NNE-SSW direction of active extension across this back-arc area located behind the Hellenic subduction zone. The study area is still affected by aftershocks, with up to now 3,192 events of magnitude  $\geq 2.0$  and 61 events of magnitude  $\geq 4.0$ . The largest aftershocks ( $M \geq 5.0$ ) occurred on 30 and 31 October 2020 and their magnitudes were estimated to be  $M_W$  5.2 and 5.0 respectively (KOERI 2020). The aftershock sequence extends over more than 70 km, both E and W of the hypocenter (Fig. 1).

As highlighted by several previous studies (MMI 2000; Bjerrum et al. 2013), into the possible consequences of large earthquakes in the region, the 30 October 2020 Samos (eastern Aegean Sea) earthquake caused significant damage to the city of Izmir, that is the third largest city in Turkey with a provincial population of 4.5 million, located approximately 70 km from the earthquake epicenter. The structural provenance of the Izmir bay is identified with related extensional tectonics in western Anatolia, and is located within the Basin and Range province (Uzel et al. 2013; Gok and Polat 2014). The city of Izmir is located on the Inner Bay of Izmir, upon the growing marine soft soil deposits. The unexpected extensive damage caused by the earthquake was, to some extent, caused by the presence of soft sediments that amplified earthquake ground motion at frequencies around 0.5-1.5 Hz and increased building damage in the Karsiyaka and Bayrakli districts in the city. Furthermore, there have been many large earthquakes ( $M > 6.5$ ) in the region with rather catastrophic consequences to the city of Izmir. The earthquake of 10 July 1688 that completely destroyed the city; earthquakes occurred in 1739 Foça and another earthquake occurred in 1788 in the Izmir area again destroyed most of the city (Ambraseys 2009; Sosyal et al. 1981). Therefore it becomes important to understand the interaction

between the main fault systems surrounding Izmir, as well as the attenuation of waves propagation through the Earth and the site specific characteristics in the metropolitan area to generate realistic estimates of seismic hazard through scenario based ground motion modeling for the future possible earthquakes.

In this study, we investigated the main features of earthquake source rupture and mechanism together with observed ground motion variability in different sites. In this respect, first we utilized Interferometric Synthetic Aperture Radar (InSAR) data acquired by the Sentinel-1 satellites and Global Positioning System (GPS) measurements to study the ground displacement field and to derive, by using elastic dislocation modelling, the fault geometry and slip distribution of the causative fault segment, that represent crucial input parameters for the ground motion simulations, especially for the areas in the near-source region. In regard to earthquake ground motion, we describe the seismic wave attenuation pattern as a function of distance and frequency from source to site taking into account earthquake source complexity as well as the local soil condition properties on ground motions. To do so we generated high-frequency strong ground motion recordings obtained during the 2020 Samos earthquake using a stochastic finite-fault simulation approach. Then we compared those with observed ground accelerations and velocities to bring detailed understanding of the damage caused in the city of Izmir (Motazedian and Atkinson 2005; Boore 2009). Several approaches such as the horizontal to vertical ratio (H/V) (Nakamura 1989), the standard spectra ratio (SSR) (Borcherdt 1970) and the frequency domain transfer function (Haskell 1960) method have been applied to estimate the fundamental soil frequency as well as the site amplifications for the stations located in the soft soils around the Izmir Bay. Both the observed and the simulated pseudo-acceleration response spectra are compared with the EC8 design spectrum and the new Turkish building code (TBSC-2018) for engineering applications.

## 2 Tectonical And Seismological Setting Of The Study Area

The Greek island of Samos is located in the eastern part of the Aegean Sea, a few kilometers west of the Turkish coast (Fig. 1). The Aegean region and western Turkey are among the most seismically and tectonically active areas in the Euro-Mediterranean region, therefore characterized by a significant seismic hazard. The current stress regime of the Samos area is associated with regional Aegean Sea NNE-SSW extension. In particular, this area represents an extensional back-arc region located behind the Hellenic subduction zone (e.g. McKenzie 1978), as a result of the ongoing movement between the Eurasian, African, Arabian and Anatolian plates (Şengör 1987; Yılmaz et al. 2000). In fact, northeast motion of the African plate underneath Greece and western Anatolia (Turkey) along the Hellenic Arc resulted in a E-W oriented rift and graben systems in the Aegean Sea, as well as in western Turkey (McKenzie 1978; Taymaz et al. 1991). This extensional crustal deformation in the region (about 7.4 mm/yr of crustal extension between Samos and western Anatolia as suggested by Vernant et al. 2014) results in various complex fault systems (a combination of normal-slip and strike-slip faults). Based on field evidence for onshore faults and on effects of faulting on the seafloor from offshore faults, different active tectonic structures have been identified in the study area (e.g. Chatzipetros et al. 2013). The coastline of Samos seems to be partly controlled by faulting: a dextral transtensional strike-slip fault striking NE-SW to the NW shoreline; a E-W striking normal fault with dextral component in the SW coastline; the Vathy WNW-ESE striking normal fault located on the NE of the island; and the approximately 30 km long, WNW-ESE striking offshore North Samos fault. The Kusadasi gulf in Turkey is bounded by an active right-lateral NS trending fault (the Gülbahçe Fault) and by NE-SW trending faults (the Seferihisar and Tuzla faults, respectively) (Ocakoğlu et al. 2004).

In historical and recent times, Samos and Turkey's west coast have experienced multiple damaging earthquakes. In the early 20th century, on 11 August 1904, a  $M$  6.8 earthquake struck the south coast of Samos causing significant damage in the Greek islands and destroying many cities in western Anatolia (Macropoulos et al. 2012). In addition, during the historical period, around 201-197 BC, 46-47 AD and between 1700 and 1799, circa ten damaging

earthquakes occurred in and around Samos (Stiros et al. 2000). Particularly, large earthquakes occurred in the region on 10 July 1688, in 1739 and 1788 with catastrophic consequences in the city of Izmir (Soysal et al. 1981; Ambraseys 2009). Recently, a series of moderate magnitude earthquakes, including the 17 October and 20 October 2005  $M$  5.7 and  $M$  5.9 earthquakes, respectively, together with the intense seismic activity observed adjacent to the southern part of the Gülbahçe Fault (Aktar 2007), caused damage to buildings in the region (Sözbilir et al. 2009). Detailed information and knowledge on these and many other events in terms of magnitude and the geometry and kinematics of the activated faults can be found in Tan et al. (2014), Chatzipetros et al. (2013), Ambraseys (2009), Kouskouna and Sakkas (2013).

## 3 Earthquake Source Model

### 3.1 Geodetic dataset

We used InSAR data acquired by the Sentinel-1 satellites in TOPS (Terrain Observation by Progressive Scans) mode and continuous GPS observations to measure the ground displacement due to the 30 October 2020  $M_W$  7.0 Samos earthquake. In particular, we used Sentinel-1 ascending interferogram made with the 23 October and 10 November 2020 scenes acquired on track 029, and the descending interferogram made with the 24 October and 11 November 2020 scenes acquired on track 136 (Figs. 2 and S1), because these 18-days pairs provide better quality interferograms than the previous pairs. Other interferograms of different tracks (i.e. ascending track 131) or with different temporal acquisition scenes were also processed, but the extracted information was of a lower quality.

The interferograms were produced using the Sentinel Application Platform SNAP software developed by the European Space Agency. The topographic phase component was removed exploiting the DEM (Digital Elevation Model) provided by Shuttle Radar Topography Mission 1 arcsec (Jarvis et al. 2008). We enhanced the signal to noise ratio of the resulting interferograms by applying the Goldstein filtering algorithm (Goldstein and Werner 1998) with a coherence threshold of 0.3. Both the interferograms show a clear fringe pattern of the coseismic displacements (Fig. S1), corresponding to ground deformation onshore on the west of Samos.

The interferograms were then unwrapped using Statistical-Cost Network-Flow Algorithm for Phase Unwrapping (SNAPHU) (Chen and Zebker 2001) and finally geocoded to obtain the ground deformation maps. In the displacements pattern, we observed a major lobe of increasing LOS (Line-Of-Sight) displacements (with maximum value of about 10-15 cm) towards the satellite in the NW Samos, except from a small sector of the NE coast of Samos, where the motion is away from the satellite (Figs. 2, S2 and S3).

In addition, we also used the GPS measurements of coseismic displacements from Ganas et al. (2020), which reveal a general relative normal motion E-W to ESE-WSW oriented between Samos and Turkey's west coast (Fig. 3), in agreement with the moment tensor solutions of both regional and teleseismic data (e.g. CSEM-EMSC). The largest horizontal and vertical static offsets were measured at SAMO site, where about 37 cm of movement towards S-SW and an uplift of about 9 cm were observed (Fig. 3), in agreement with InSAR data.

### 3.2 Inversion for fault geometry and coseismic slip

To image the fault geometry and slip distribution of the 2020 Samos mainshock, we simply inverted the static deformation for distributed slip on a number of different fault geometries, corresponding to a NNE-dipping fault rupture scenario. We adopted the same inversion scheme as in Cheloni et al. (2019), which used rectangular dislocations embedded in an elastic, homogeneous and isotropic half-space (Okada 1985). Before modelling, the InSAR interferograms were downsampled to reduce the number of data points from several millions to a set of about some

hundreds of points, using a resolution-based resampling algorithm (Lohman and Simons 2005; Figs. S2 and S3). The geodetic data is thus inverted for slip magnitude on each fault patch of constant rake and size (2.5 km × 2.5 km), inferring the optimal fault geometry iterating by grid searching over, locations, strikes, dips and rake angles of the fault plane jointly inverting InSAR LOS and GPS displacements, while using relative weights to properly combine the different data sets (Fig. S4). We also used positivity constraints in the inversions using a bounded-values, weighted least-squares algorithm (Stark and Parker 1995) to impose positivity constraints on the estimated slip and we regularized the linear inversion by applying spatial smoothing (Fig. S5). Additional terms consisting of a linear ramp for each InSAR interferogram are also included in the inversion to minimize the effect on the solution of any residual long-wavelength orbital signal in InSAR images.

The inversion of the geodetic displacements satisfactorily reproduces both the observed InSAR LOS displacement maps (Fig. 2) and the GPS offsets (Fig. 3). The best-fitting fault model is obtained with N285°ESE-WNW striking and 38°NNE dipping normal (rake angle equal to -80°) fault plane in good agreement with focal solutions and with the distribution of aftershocks (Fig. 4). The coseismic slip distribution model on the preferred fault plane (50 km × 25 km; including 20 × 10 sub-faults) shows a single major asperity with peak slip of about 2.5-3 m, located WNW respect to the epicentre, for an along-strike length of about 40 km. Although a detailed fine slip distribution cannot be obtained from the available geodetic dataset (due to the lack of measurements at sea), nevertheless, the obtained slip distribution is compatible with aftershocks location, which is characterized by the almost complete absence of seismic events in the area where we retrieved most of the slip, suggesting therefore that the largest slip may have occurred just in this region. The resulting seismic moment is  $3.3 \times 10^{19}$  Nm, corresponding to a  $M_W$  7.0 earthquake, in agreement with seismological results. Our retrieved slip distribution located westward of the epicenter, implies therefore a predominantly WNW rupture directivity. Our preferred fault plane geometry and the dimension and positions of the main slip asperity agree also with the recent study of Ganas et al. (2020), who suggest that rupture during the Samos earthquake occurred on a 37 km NNE dipping normal fault located offshore of the north coast of Samos. These source related parameters are crucial to predict the ground motions particularly in near source.

## 4 Investigating The Strong Ground Motion Characteristics Of The 30 October 2020 Earthquake Through Synthetic Seismograms

### 4.1 Strong ground motion dataset and some observations

Strong motion data were obtained mostly from the networks managed by the General Director of Disaster Affairs, Earthquake Research Department (AFAD) and the Bogazici University, Kandilli Observatory and Earthquake Research Institute (KOERI). AFAD stations are mostly well documented (AFAD 2020) and contain lots of information on the  $V_{s30}$ , the average velocity over the top 30 m of the soil at each station, the fundamental resonant frequencies ( $f_0$ ) and the corresponding soil types according to European Seismic Design Codes, EC8 (CEN 2006). Although the distribution of the accelerometers deployed in the epicentral area seems very few, the earthquake registered approximately 200 strong motion records within 250 km of the fault (Fig. 1). Few strong motion stations registered the mainshock in Samos Island (KRL1, SMG1 and SAMA). The maximum observed peak ground acceleration (PGA) was around 0.23 g and 0.27 g in Samos at SMG1 and on the southern tip of the Karaburun Peninsula at GMLD (KOERI) strong motion stations, respectively. These stations are the closest to the epicenter, being located around 17 km to the south and 22 km to the northwest of the mainshock. The station 0905, located 43 km from the fault plane and on stiff soil, recorded 0.18 g peak ground acceleration, the second highest after the GMLD station. Most of the stations positioned in Izmir have relatively low ground accelerations with values near 0.1 g, while those stations located on the soft soil of the Bayraklı and Karsiyaka districts of the city have amplified ground motions for longer periods. In Table 1 the strong ground

motion stations are given, along with the station name, location, site class (according to the EC8 classification), source-to-site distances, and the observed peak ground accelerations and peak ground velocities at three components.

## 4.2 Generation of synthetic strong ground motions

In this section, to better understand the ground motion characteristics and the physical processes and parameters underlying seismic wave propagation of the 30 October 2020 Samos earthquake, we composed a stochastic ground motion model to generate predictions of peak ground acceleration and velocity, and 5%-damped response pseudo-spectral acceleration for the  $M_w$  7.0 mainshock. These simulations account for source, path and site effects related to the fault rupture, the seismic wave propagation as well as the complex site responses in the case of the sedimentary basin, providing a spatial variation of ground motion, which may be essential to assess the seismic hazard and reduce the seismic risk in the populated urban areas.

The strong ground motion synthetics were completed by using a stochastic finite-fault simulation model, based on dynamic corner frequency (Motazedian and Atkinson 2005; Boore 2009). Stochastic simulation methods contemplate the physics-based rupture process and call for well-defined source and slip distribution, together with path, and local site conditions within the region of interest.

The finite-fault source model with slip distribution (Fig. 4a) determined in the present study is intended as an input to the ground motion calculations (see previous section and Table 2). The region specific crustal S waves attenuation parameters are selected as characterized by Akinci et al. (2012), using several hundred regional earthquakes ( $M$  2.5-5.8) recorded during the Western Anatolia Seismic Recording Experiment (WASRE) between November 2002 and October 2003 (Akyol et al. 2006; Zhu et al. 2006). The anelastic attenuation for the entire region is given as the quality factor,  $Q_s(f) = 180f^{0.55}$  and the geometrical spreading coefficient,  $g(r)$ , occurring at a hypocentral distances of 20 and 40 km which changes from a body-wave-like function  $g(r) \propto r^{-1.0}$  to  $g(r) \propto r^{-0.8}$  and  $g(r) \propto r^{-0.5}$  expected for surface waves for distances larger than 100 km. These results are quite similar to that obtained by Kurtulmus and Akyol (2013) as  $Q_s(f) = 190f^{0.64}$  with a rapid decay of  $g(r) \propto r^{-1.0}$  both for short and long distance ranges in the same region. The stress drop parameter was determined from the residuals between the observed and the simulated peak ground accelerations which were calculated using different  $\Delta\sigma$ , ranging from 50 to 200 bars (Fig. S6). As observed in Figure S6, a stress drop value of  $\Delta\sigma = 80$  bars was considered as the most reasonable value to provide a satisfactory comparison, with lower residuals. This value is also in good agreement with those determined with earthquakes of similar magnitude in Turkey. The level of the acceleration spectrum at high frequencies is estimated between 8-20 MPa by Akinci et al. (2006, 2014), Cheloni and Akinci (2020) and Malagnini et al. (2010) for the 1999 Kocaeli  $M_w$  7.2 and 2020 Elazig (Doganbey)  $M_w$  6.8 earthquakes with strike-slip faulting, respectively, and for the 2011 Van Lake  $M_w$  7.1 earthquake with reverse faulting in Turkey.

The parameters employed to quantify the impact of the shallower sedimentary layers to the seismic ground motion are the soil amplification factor  $D(f)$  and the kappa parameter ( $\kappa$ ). The former is characterized as an exponential decay to produce the diminution factor,  $e^{-\pi f \kappa}$  (Anderson and Hough 1984). In the present study, we used frequency-dependent generic site amplifications and kappa parameters for different site classes from Boore and Joyner (1997) and Pischiutta et al. (2020). The  $\kappa$  parameter was set as 0.035 s for the site class A (average  $V_{s30}$  1150 m/s, Pischiutta et al. 2020) and B ( $V_{s30}$  between 620 m/s, Boore and Joyner 1997), while for the site class C and D (average  $V_{s30}$  255 m/s and 190 m/s), it was favored as 0.055 s.

The physical parameters that characterize the earthquake source rupture and the seismic wave propagation together with the site related parameters considered to generate synthetic ground motions are listed in Table 2, while the generic site amplifications are given in Table S1. We note that the adopted generic site amplifications, calculated through the quarter wavelength approach (Joyner and Fumal 1985; Boore and Joyne, 1997) using the averaged velocity over the uppermost 30 m of the soil, and are characterized by velocity gradients which are not sensitive to impedance contrasts between the layers (Boore et al. 1994, 2011). In the following section, to give more attention to this topic, we evaluated local site responses in terms of spectral amplification by using several different techniques, particularly for sites located in the Karsiyaka and Bayrakli districts where heavy damage was observed during the 30 October 2020 earthquake (Erdik et al. 2020).

## 4.3 Spatial distribution of horizontal peak ground accelerations and velocities

In order to investigate the spatial distribution of the ground motions we simulated the  $M_W$  7.0 Samos earthquake at 1055 virtual stations distributed on a regular grid with 5-km spacing together for the sites where strong ground motion stations were actually located. In Figures 5a and b we presented the spatial distribution of the PGA and PGV values obtained from the simulations using the main fault rupture and the spectral parameters (Table 2) within the selected area using a uniform rock site amplification with  $V_{s30} = 760$  m/s referring to the engineering bedrock. The spatial distribution of simulated PGA and PGV values for the 30 October 2020 mainshock holds explicit effects of the earthquake source rupture since the soil condition is assumed to be uniform across the region. The strongest ground shaking is observed in areas close to the main asperity with a larger slip located roughly in the central part of the fault and calculated around 0.5 g in PGA and 50 cm/s in PGV in the northwest of Samos. Simulations at the nearest stations, GMLD at  $R_{jb} = 11$  km and 0905 at  $R_{jb} = 21$  km resulted in PGA of 0.23 g, and 0.15 g while observed values range from 0.19-0.27 g, and 0.15-0.18 g, respectively. There is good consistency found between observed and predicted ground motions close to the source rupture, which confirms the well constrained source parameters (fault geometry and slip distribution) described in the present study. Simulated ground motions are then somewhat validated by the observed ground motion parameters and compared with two selected ground motion prediction equations (GMPEs), in terms of PGA and PGV values, for epicentral distances up to 250 km.

## 4.4 Comparisons between observed and simulated time histories and Fourier Spectra

In this section to demonstrate the efficacy of our ground motion model both in time and frequency domain, we compared some selected recordings of acceleration and velocity time histories and their Fourier Amplitude spectra with synthetic ones. In our simulations we examined different geological conditions for each strong motion station according to the network classification (Table 1). As shown in Figure 6a the synthetic time series are in rather good agreement with those of the selected recordings considering only generic site amplification factors were used. Although the synthetic spectra match quite well with those of the recorded data, especially at most of the stations located on rock and stiff soil, reproducing acceptable amplitudes and frequency content, they underestimate spectral amplitudes between 0.5 and 2.0 Hz for those recordings observed at stations located in the Bornova Basin, Izmir (Fig. 6b). Stations 3519, 3513, 3521 and 3518 are located on alluvial sites close to the shoreline of the Bayrakli and the Karsiyaka district whereas stations 3514, 3524, 3521 are deployed on the stiff soil site in Izmir. As can be observed in Figure 6a the stations 3519, 3513, 3521 and 3518 have longer periods and higher amplitudes due to their local site characteristics. In fact, a considerable part of the metropolitan area of Izmir is located on sedimentary alluvial deposits. Furthermore, the

notable fluvial degradation takes place in the delta of the Gediz River in the northern section of the İzmir Bay (Uzel et al. 2013). Therefore, the use of the generic site amplifications may not be enough to properly quantify the site amplification factors since they disregard specific geological features of the soil stratigraphy such as the impedance contrasts in sedimentary basins and the soil depths. Although the generic soil amplifications have been used commonly in many applications, Boore (2013) has exposed their limitations inferred by the method, the quarter wavelength approach, which smooths so that underestimates of the fundamental resonant peaks generated by the presence of the strong bedrock/soil seismic impedance contrasts. In addition, several studies have also indicated the importance of the soil/bedrock impedance contrast, thickness of soil, and soil properties on characterizing the site response in terms of amplitude and frequency content (Zandieh and Pezeshk 2011; Banab et al. 2012; Molnar et al. 2004). For example, Pratt et al. (2017) have demonstrated that the strong ground motion amplifications generated by the strong contrasts between shallow sediments and underlying bedrock beneath Washington, D.C., during the relatively distant and moderate size  $M_W$  5.8 Virginia earthquake. Particularly, Baise et al. (2016) stated that the short- and intermediate-period amplification considered in building codes may underpredict soil amplification in strong impedance contrast environments such as in Boston, Massachusetts.

## 4.5 Comparison between observed, simulated and predicted GMPEs ground motions

Finally, the simulated horizontal peak accelerations and velocities have been compared with those from processed data of the 30 October Samos earthquake together with some ground motion prediction equations (GMPEs) developed on the basis of strong motion data. The two GMPEs are preferred being 1) the local GMPE, Akkar and Cagnan (2010) (hereafter AC10) derived from the Turkish strong motion recordings and 2) the global NGA-west model of Boore et al. (2014) (hereafter BSS14) derived based on metadata from shallow earthquakes in tectonically active regions in the world. The relations are derived for normal faulting style and for engineering rock site conditions,  $V_{s30} = 760$  m/s, to be comparable and to fit the conditions in this study. We employed different generic site amplifications and kappa factors in the calculations which are assigned on the basis of the soil classification according to the EC8 (Tables 1 and 2). Both the recorded and simulated peak accelerations and velocities at distances up to 250 km from the fault are compared with the two selected empirical GMPEs (Figs. 7a and b). We also gathered the simulation ground motion parameters performed for the generic soil site class at the 1055 virtual stations to those simulated for the 116 strong motion stations of the AFAD network on different geological conditions. Generally, the ground motions obtained from simulations agree well with the observed ground motion parameters although the recordings present larger non-conformity over greater distances  $R_{jb} > 100$  km. The observed PGAs and PGVs are mostly in the range of the empirical relationships for the BSSA14 and the AC10 yet, the BSSA14 model better predicts the observed peak accelerations and velocities at distances over 100 km with respect to the AC10. At the closest  $R_{jb}$  distances (up to 20 km), simulated PGA and PGV values present a large variability and have a more scattered data distribution compared to the variations provided by the empirical relationships with one standard deviation. Because the simulated PGAs and PGVs acquired from normal faulting mechanism represent large variation between the hanging-wall and foot-wall section of the fault plane. Maximum acceleration values at the closest distances range between 0.5 and 0.8 g on the hanging-wall of the fault plane.

Moreover, we observed a clear trend of the observed data due to the EC8 soil type classification up to distances of 100 km. The consequences of site effect become more evident over longer periods on PGV parameters with respect to PGAs around the 50 km  $R_{jb}$  distances. Most of the highest PGA and PGV values correspond to stations belonging to C site class located on the Bornova basin in İzmir and are remarkably underestimated by the GMPEs. The generic

amplification factors, used in our simulations, were also not able to capture properly locally amplified ground motions at particular frequencies.

## 4.6 Site amplifications

In order to completely understand the ground motion characteristics of the earthquake throughout synthetics, we investigated site characteristics of strong motion stations located on the shorelines of the city of Izmir. Particularly we examined the stations 3519, 3513, 3518, 3521 with site classification C and D, and the stations 3514, 3524, 3511 and 3520 with site classification A and B type. Site amplification factors are estimated over commonly used methods: 1) horizontal-to-vertical component spectral ratios, HVSR (e.g. Nakamura 1989; Lermo and Chavez-Garcia 1993); 2) standard spectral ratio, SSR (Borcherdt 1970); and 3) the propagator-matrix method, PMM, of Haskell (1960) and the quarter wavelength, QWL techniques (Joyner and Fumal 1985; Boore and Joyner 1997).

To determine the frequency-dependent amplifications, first of all, the ratio of the horizontal-to-vertical (H/V) components of ground motion are calculated between the horizontal Fourier spectrum (N-S and E-W spectra) and the vertical one over the S-wave; starting 1.0 s before the manually picked S-wave arrivals and over around 15-20 s time windows.

The SSR technique is applied to the recordings of the mainshock as a secondary approach to investigate the soil amplifications at the selected sites. The spectral ratio is obtained by dividing the Fourier spectrum of the acceleration for the S wave at the selected stations by the spectrum of the S wave at the reference stations on the hard-rock sites. The station 3514 is chosen as a reference station being deployed on a geologic bedrock ( $V_{s30} = 836$  m/s).

In order to interpret the site amplifications based on shear wave velocity, density and attenuation as a function of depth, as a tertiary approach we computed the theoretical amplifications for three sites using the propagator-matrix method of Haskell (1960). To do so we used the *site\_amp* and *nrattle* computer program, a modified version of C. Mueller's program *rattle* by R. B. Herrmann (part of the SMSIM computer codes of Boore 2003). We prototyped shear-wave velocities and attenuation as a function of depth from those profiles provided by Pamuk et al. (2018, 2018b) and computed amplifications in the frequency-domain. In these velocity models, engineering bedrock ( $V_s > 760$  m/s) depth changes from 200 to 400 m in the Bornova basin while the seismic bedrock ( $V_s > 3000$  m/s) ranges between 1200 to 1400 m. The velocity profiles S2, S3, S5 and the deeper one S4, with greater proximity to the 3519 station, are adopted from Pamuk et al. (2018). Figure 8a shows adopted 1D prototyped  $V_s$ -depth profiles (see Figure 5 of Pamuk et al. 2018) and Figure 8b shows amplifications with a vertical incidence wave of geometrical effect calculated using the PPM (continuous lines) and QWL (dashed lines) methods. Attenuation effect at the closest sites is included using kappa parameters 0.055 s. As can be seen clearly in Figure 8b, the QWL method underestimates the resonance peaks generated by the large impedance contrasts. The resonant frequencies are different based on the four models and the shear wave profiles considered for the site amplifications. The site responses derived from the PPM are double those obtained from the QWL one. There is also clear evidence that the maximum peak value is shifted towards lower frequencies when the thickness of the layer increases. The S4 model with a strong impedance variation at roughly 120 m and 600 m presents larger peaks around 0.7 and 1.6 Hz yet the frequency of resonant peak decreases, 0.3 s, with increasing thickness, having a relevant impedance contrast around 450 m, in the case of the velocity model S3.

In Figures 9a and b we compare the resultant site amplifications from HVSR (left six panels) and SSR methods (right six panels): it is evident the strong amplifications at stations 3519, 3513, and 3521 with a clear peak at low frequencies between 0.3 and 1.5 Hz, while stations located on rock and stiff soil do not show any evidence for strong amplifications at least for frequencies lower than 3-4 Hz. These clear and sharp peaks may imply the presence of firm velocity

contrast at depth between unconsolidated deposits and underlying bedrocks. From Figure 9, we can conclude that the surface/bedrock ground motion felt at the station 3519 was 5-8 times larger in respect to that at station 3514 at the fundamental period of 0.7 s. Amplification values obtained from the HVSR method are slightly greater, roughly at low frequencies, than the SSR results. Site amplifications from theoretical experiments of the quarter-wavelength approximation confirm the suggestion that the maximum amplitude of spectral ratios is sensitive to relevant impedance contrasts.

Although the three methods were able to closely reveal the fundamental frequencies, all being ranged between 0.3 and 2.0 Hz, they provide relatively different results concerning the amplitude of ratios. This could be due to several factors such as the amplified vertical component by the multiple reflected and converted waves by basin geometry or the selected reference station which does not have a perfectly flat spectrum and may be explored in future studies. Finally, in Figure 10 we demonstrated the effect of site amplifications obtained from the PPM and the QWL approximations throughout our simulations. We computed spectral accelerations at three sites 3519, 3513 and 3520, located on the soft soils and compared those with the observed spectral accelerations. Simulated spectral accelerations calculated using the site response spectra obtained from the PPM fit well with the observed data reproducing resonant peaks and corresponding amplitudes. However, these resonance peaks are always underestimated by the QWL amplifications since the method is insensitive to the important impedance contrasts between layers and the velocities are averaged over depth. In the Supplementary Material we further provided some synthetic time series and their complementary Fourier spectrum calculated using site responses with the resonance peaks (Fig. S7).

## 4.7 Acceleration response spectra and observed damage distribution in the Metropolitan area of Izmir

In general, the damage potential of the ground motions on the structures are measured by the amplitudes and shape of the response spectrum. Buildings are designed withstand forces no higher than these spectral values. To examine the effect of the earthquake on the Izmir Metropolitan area, we compared code compiled spectrum with the spectra computed from the recorded ground motions. Figure 11 shows the spectral accelerations (response spectra, 5% damping) computed from the NS and EW components recorded at eleven stations, with five and six being located on soft and rocky soil sites within the study area. In the same figure, previous (TSC-2007) and most recent uniform seismic hazard spectra (TBSC-2018) were also depicted. Upper boundaries of the design-level spectrum of TSC-2007 and TBSC-2018 are almost identical at hard soil station locations except for 3512 and 3524 stations both having higher spectral values in TBSC-2018. With regards to soft soil stations, TBSC-2018 spectra are approximately 19% percent higher than TSC-2007 values. Except for in the vicinity of the 0.5 - 1 sec periods which reflect the dominant vibration period of 5-10 story reinforced concrete buildings, the spectral values of the recorded motions (average of the spectral values at 1s period for soft and hard soil stations are 0.37 g and 0.10 g, respectively) are far below the design-level spectra (0.57 g and 0.22 g for soft and hard soils, respectively) of the recent earthquake building codes. Therefore, buildings would have neither suffered from any excessive damage, nor collapsed if they had been constructed according to the engineering practice and design guidelines.

Following the 30 October 2020 Samos earthquake, the Ministry of Urbanization and Environment completed on-site assessment of the building inventory in Izmir to determine the condition of the structures and share the assessment reports on the website (MUE 2020) for possible reclamations by the property owners. The spatial representation of the distribution of the damaged buildings acquired from the reports is plotted in Figure 11 in order to correlate the soil condition and computed spectral values of the records. Two important morphological features are clearly observable, associated with the high bedrock outcrops and with the low-lying basin structure with thick sedimentary deposits. A

considerable part of İzmir's metropolitan area is located on sedimentary alluvial deposits. Furthermore, the notable fluvial degradation takes place in the delta of the Gediz River in the northern section of the Bay of İzmir. During the 30 October earthquake, site response played an important role in the amplification of ground motions on soft soil sites such as 3513, 3518, 3519, 3521 and 3522 sites (Fig. 12).

Izmir is one of Turkey's major cities, where migration in the last couple of decades increased significantly. Thus, rapid housing demand has been a critical issue in which the construction quality and proper engineering design has been compromised. Catastrophic results of the soil amplification and the inadequate construction techniques were the main issues in the İzmir Earthquake Master Plan (MMI 2000) where the areas have already been highlighted as having the potential for significant building damage (Fig. 13).

Similarities between the predicted and observed distribution maps reveal the necessity of considering the local site conditions and also housing demand in accordance with population growth must be explicitly included in the urbanization plans. On the other hand, the assessment reports and observations on the site indicate that the damaged buildings during the earthquake were constructed with low quality material and workmanship which are crucial defects of the construction sector in the developing countries. To avoid further damage, the Ministry of Environment and Urbanization decreed to demolish all buildings with major to moderate damage (as of December 2020, 652 and 778 major and moderate damaged buildings, respectively) as well as the surrounding buildings if constructed by the same contractors. The damage distribution due to the earthquake clearly reveals all engineering steps including soil examination, soil-structure interaction in terms of resonance frequency, code-complied design and construction must be substantially considered in urbanization policies.

## 5 Conclusion

In this study we provided a complete description of the strong ground motions induced by the 30 October 2020  $M_w$  7.0 Samos (eastern Aegean Sea) earthquake taking into account three principal components that characterize the observed ground motions (earthquake source complexity, seismic wave propagation and site effects) through the earthquake simulations. Although we studied each of the physical parameters and the consequences on the predicted ground motion, particular attention was given to interpretation of the observed ground motions in terms of the site effects that played a particular role in the Bay of İzmir area.

With regards to the seismic source, the Samos earthquake was caused by the rupture of a NNE-dipping normal fault located offshore of north coast of Samos. The geometry and location of our preferred model is therefore consistent with the rupture of the offshore North Samos Fault during the main seismic event, which was believed to be active mainly on the basis of its effect on the seafloor (Chatzipretos et al. 2013). The slip distribution obtained from the inversion of geodetic data shows a main asperity (peak slip of about 2-5-3 m), located WNW from the epicenter, suggesting therefore a westward directivity during the mainshock. The seismic moment release is  $3.3 \times 10^{19}$  Nm (equivalent to a  $M_w$  7.0), in agreement with magnitude estimates provided by different research Institutes.

Our results indicate that the detailed knowledge of the regional crustal and near-site specific attenuations as well as the earthquake source rupture characteristics, are essential for a complete understanding of the earthquake induced seismic hazard and to better predict the earthquake ground motions in a region. Region specific frequency-dependent attenuation together with the geometrical-spreading coefficient as described by Akinci et al. (2013) are successfully used to simulate ground motions in the study area.

We demonstrated that the generic soil amplifications used for the simulations were not adequate for the soil and the site conditions in İzmir Bay where simulations systematically underestimate the observed ground motions at the period

range of 0.5 to 1.5 s. Stations located within the Bornova basin are characterized by the largest estimates of the amplification amplitudes at that particular period range that are commonly detected by the three different approximation methods (HVSr, SSR and PPM). Conversely, stations located on the rock units show the least amplification level, ranging between 2 and 4. We have obtained substantial improvements on our simulations by considering the strong resonance effects particularly at lower frequencies ( $f < 1.5$  Hz).

Damage to the city of Izmir exhibits that small-to-moderate ground motions can be locally amplified modifying the intensity of ground shaking. Since these amplified waves may cause structural damage, a proper calibration of the site response is fundamental not only for ground motion simulations, but also for site classifications throughout the Izmir Bay area. The peculiar resonant frequencies of ground shaking this need to be taken into consideration when undertaking the seismic-resistant design of civil engineering structures in the Izmir Metropolitan area, where the annual rate of construction of residential buildings has increased five fold (from 1500s to 7500s per year) over the last 18 years (TSI 2021). Furthermore, active tectonic structures and historical seismicity of the area suggest that earthquakes with similar size may occur close to the city again in the future, and could produce much greater damage in the area.

## Declarations

**Acknowledgement** Most of the figures have been created using the Generic Mapping Tool version 4.2.1 ([www.soest.hawaii.edu/gmt](http://www.soest.hawaii.edu/gmt)) and the Seismic Analysis Code (SAC) software IRIS SeisCode ([washington.edu](http://www.washington.edu)). We use Copernicus Sentinel-1 InSAR imagery (<https://scihub.copernicus.eu/>). Sentinel-1 data are copyright of Copernicus (2020). We thank Athanassios Ganas of the National Observatory of Athens for sharing GPS data. The strong motion data used in this study were obtained from the Earthquake Department of the Disaster and Emergency Management Presidency, AFAD, Kandilli Observatory and earthquake Research Institute, KOERI. We thank everyone who contributed to this matter. We thank Gail Atkinson, Dariush Motazedian, and David Boore for providing the computer code to generate ground motion simulations (*EXSIM*). Some of the amplifications are computed using the programs *site\_amp* and *nrattle*, available from the online software link at [www.daveboore.com](http://www.daveboore.com). Authors would like to thank Simon J. Ellis for correction of English style, grammar and spelling. We thank R. B. Herrmann from Saint Louis University for his helpful contribution on the earthquake magnitude and the moment tensor solution.

### Funding

No funding was provided for the development of the manuscript.

### Conflicts of interest/Competing interests (include appropriate disclosures)

It's declared that no conflict of interest or competing interest between the authors and/or third person(s).

### Availability of data and material (data transparency)

Data and material could be provided upon request to the first author of the manuscript.

### Code availability (software application or custom code)

David M. Boore Online Software ([daveboore.com](http://daveboore.com))

## References

AFAD (2020) Turkish Accelerometric Database and Analysis System. <https://tadas.afad.gov.tr/eventdetail/11995>. Accessed 20 Nov 2020.

- Akinci A, Malagnini L, Herrmann RB, Kalafat D (2014) High-Frequency Attenuation in the Lake Van Region, Eastern Turkey. *Bulletin of the Seismological Society of America* 104:1400–1409. doi: 10.1785/0120130102
- Akinci A, D'Amico S, Malagnini L, Mercuri A (2013) Scaling earthquake ground motions in western Anatolia, Turkey. *Physics and Chemistry of the Earth, Parts A/B/C* 63:124–135. doi: 10.1016/j.pce.2013.04.013
- Akinci A, Antonioli A (2012) Observations and stochastic modelling of strong ground motions for the 2011 October 23 Mw 7.1 Van, Turkey, earthquake. *Geophysical Journal International* 192:1217–1239. doi: 10.1093/gji/ggs075
- Akinci A, Malagnini L, Herrmann RB, et al (2006) Ground motion scaling in the Marmara region, Turkey. *Geophysical Journal International* 166:635–651. doi: 10.1111/j.1365-246x.2006.02971.x
- Aktar M, Karabulut H, Özalaybey S, Childs D (2007) A conjugate strike-slip fault system within the extensional tectonics of Western Turkey. *Geophysical Journal International* 171:1363–1375. doi: 10.1111/j.1365-246x.2007.03598.x
- Akyol N, Zhu L, Mitchell BJ, et al (2006) Crustal structure and local seismicity in western Anatolia. *Geophysical Journal International* 166:1259–1269. doi: 10.1111/j.1365-246x.2006.03053.x
- Ambraseys NN (2009) *Earthquakes in the Mediterranean and Middle East: a multidisciplinary study of seismicity up to 1900*. Cambridge University Press ISBN: 978-0-521-87292-8
- Anderson JG, Hough SE (1984) A model for the shape of the Fourier amplitude spectrum of acceleration at high frequencies. *Bull Seismol Soc Am* 74:1969–1993
- Baise LG, Kaklamanos J, Berry BM, Thompson EM (2016) Soil amplification with a strong impedance contrast: Boston, Massachusetts. *Engineering Geology* 202:1–13. doi: 10.1016/j.enggeo.2015.12.016
- Banab KK, Kolaj M, Motazedian D, et al (2012) *Seismic Site Response Analysis for Ottawa, Canada: A Comprehensive Study Using Measurements and Numerical Simulations*. *Bulletin of the Seismological Society of America* 102:1976–1993. doi: 10.1785/0120110248
- Bjerrum LW, Sørensen MB, Ottemöller L, Atakan K (2013) Ground motion simulations for İzmir, Turkey: parameter uncertainty. *Journal of Seismology* 17:1223–1252. doi: 10.1007/s10950-013-9389-9
- Boore DM, Joyner WB, Fumal TE (1994) Estimation of response spectra and peak accelerations from western North American earthquakes: An interim report, Part 2, U.S. Geol. Surv. Open-File Rept. 94-127, 40 pp.
- Boore DM, Joyner WB (1997) Site amplification for generic rock sites. *Bull Seismol Soc Am*, 87:327–341
- Boore DM (2003) Simulations of ground motion using the stochastic method, *Pure and Applied Geophysics* 160, 635/675.
- Boore DM (2009) Comparing Stochastic Point-Source and Finite-Source Ground-Motion Simulations: SMSIM and EXSIM. *Bulletin of the Seismological Society of America* 99:3202–3216. doi: 10.1785/0120090056
- Boore DM, Thompson EM, Cadet H (2011) Regional Correlations of VS30 and Velocities Averaged Over Depths Less Than and Greater Than 30 Meters. *Bulletin of the Seismological Society of America* 101:3046–3059. doi: 10.1785/0120110071
- Boore DM (2013) The Uses and Limitations of the Square-Root-Impedance Method for Computing Site Amplification. *Bulletin of the Seismological Society of America* 103:2356–2368. doi: 10.1785/0120120283

Boore DM, Stewart JP, Seyhan E, Atkinson GM (2014) NGA-West2 Equations for Predicting PGA, PGV, and 5% Damped PSA for Shallow Crustal Earthquakes. *Earthquake Spectra* 30:1057–1085. doi: 10.1193/070113eqs184m

Borcherdt RD (1970) Effects of local geology on ground motion near San Francisco Bay. *Bull Seismol Soc Am*, 60:29–61

CEN (2006) EN1998-1: Design of structures for earthquake resistance, Part 1: General rules, seismic actions and rules for buildings, Brussels: European Committee for Standardization; 2006

Cetin OK, Mylonakis G, Sextos A, Stewart JP (2020) Seismological and Engineering Effects of the M 7.0 Samos Island (Aegean Sea) Earthquake, Geotechnical Extreme Events Reconnaissance Association: Report GEER-069, <https://doi.10.18118/G6H88>

Chatzipetros A, Kiratzi A, Sboras S, et al (2013) Active faulting in the north-eastern Aegean Sea Islands. *Tectonophysics* 597-598:106–122. doi: 10.1016/j.tecto.2012.11.026

Cheloni D, Falcucci E, Gori S (2019) Half-Graben Rupture Geometry of the 30 October 2016 MW6.6 Mt. Vettore-Mt. Bove Earthquake, Central Italy. *Journal of Geophysical Research: Solid Earth* 124:4091–4118. doi: 10.1029/2018jb015851

Cheloni D, Akinci A (2020) Source modelling and strong ground motion simulations for the 24 January 2020, Mw 6.8 Elazığ earthquake, Turkey. *Geophysical Journal International* 223:1054–1068. doi: 10.1093/gji/ggaa350

Chen CW, Zebker HA (2001) Two-dimensional phase unwrapping with use of statistical models for cost functions in nonlinear optimization. *J Opt Soc Am*, 18(2):338-351

Çubuk-Sabuncu Y, Taymaz T, Fichtner A (2017) 3-D crustal velocity structure of western Turkey: Constraints from full-waveform tomography. *Physics of the Earth and Planetary Interiors* 270:90–112. doi: 10.1016/j.pepi.2017.06.014

Duman TY, Çan T, Emre Ö, et al (2018) Seismotectonic database of Turkey. *Bulletin of Earthquake Engineering* 16:3277–3316. doi: 10.1007/s10518-016-9965-9

Ganas A, Panagiotis E, Briole P, Tsironi V, Valkaniotis S, Escartin J, Karasante I, Efstathiou E (2020) Fault responsible for Samos earthquake identified. *Temblor*, <http://doi.org/10.32858/temblor.134>

General Directorate of Mineral Research and Exploration, Geology Map, <http://yerbilimleri.mta.gov.tr/anasayfa.aspx>, Accessed Dec 2020 (in **Turkish**)

Gok E, Polat O (2014) An assessment of the microseismic activity and focal mechanisms of the Izmir (Smyrna) area from a new local network (IzmirNET). *Tectonophysics* 635:154–164. doi: 10.1016/j.tecto.2014.08.003

Erdik M, Ansal A, Aydinoglu N, Barka A, Yuzugullu O, Birgoren G, Sesetyan K (2000) Development of earthquake masterplan for the municipality of Izmir. In the International Conference on Seismic Zonation

Erdik M, Demircioğlu MB, Cüneyt T (2020) Forensic analysis reveals the causes of building damage in İzmir in the Oct. 30 Aegean Sea earthquake. *Temblor*, <http://doi.org/10.32858/temblor.139>

Haskell NA (1960) Crustal reflection of plane SH waves. *J Geophys Res*, 65:4147–4150

Jarvis A, Reuter HI, Nelson A, Guevara E (2008) Hole-filled SRTM for the globe, version4, CGIAR-CSI SRTM 90m Database, available at <http://srtm.csi.cgiar.org>

- Joyner WB, Fumal TE (1985) Use of measured shear-wave velocity for predicting geologic site effects on strong ground motion, in Proc. Eighth World Conf. on Earthquake Eng., San Francisco, Vol. 2, 777–783
- Goldstein RM, Werner CL (1998) Radar interferogram filtering for geophysical applications. *Geophysical Research Letters* 25:4035–4038. doi: 10.1029/1998gl900033
- Kouskouna V, Sakkas G (2013) The University of Athens Hellenic Macroseismic Database (HMDB.UoA): historical earthquakes. *Journal of Seismology* 17:1253–1280. doi: 10.1007/s10950-013-9390-3
- Kurtulmuş TÖ, Akyol N (2013) Crustal attenuation characteristics in western Turkey. *Geophysical Journal International* 195:1384–1394. doi: 10.1093/gji/ggt318
- Lermo J, Chávez-García FJ (1993) Site effect evaluation using spectral ratios with only one station. *Bull Seismol Soc Am* 83:1574-1594
- Lohman RB, Simons M (2005) Some thoughts on the use of InSAR data to constrain models of surface deformation: Noise structure and data downsampling. *Geochemistry, Geophysics, Geosystems*. doi: 10.1029/2004gc000841
- Makropoulos K, Kaviris G, Kouskouna V (2012) An updated and extended earthquake catalogue for Greece and adjacent areas since 1900. *Natural Hazards and Earth System Sciences* 12:1425–1430. doi: 10.5194/nhess-12-1425-2012
- McKenzie D (1978) Active tectonics of the Alpine-Himalayan belt: the Aegean Sea and surrounding regions. *Geophys J Roy Astr Soc*, 55(1):217-254
- Metropolitan Municipality of İzmir (MMI) (2000) İzmir earthquake masterplan. Metropolitan Municipality of İzmir publication, İzmir, Turkey. <http://www.izmir.bel.tr/izmirdepem/izmirrapor.htm>. Last accessed 11 Jan 2021. **(in Turkish)**
- Ministry of Urbanization and Environment, Assessment Reports, <https://hasartespit.csb.gov.tr/>, Accessed on 14 Dec, 2020 **(in Turkish)**
- Malagnini L, Nielsen S, Mayeda K, Boschi E (2010) Energy radiation from intermediate- to large-magnitude earthquakes: Implications for dynamic fault weakening. *Journal of Geophysical Research*. doi: 10.1029/2009jb006786
- Molnar S (2004) Site Response in Victoria, British Columbia, from Spectral Ratios and 1D Modeling. *Bulletin of the Seismological Society of America* 94:1109–1124. doi: 10.1785/0120030195
- Motazedian D (2005) Stochastic Finite-Fault Modeling Based on a Dynamic Corner Frequency. *Bulletin of the Seismological Society of America* 95:995–1010. doi: 10.1785/0120030207
- Nakamura Y (1989) A method for dynamic characteristics estimation of subsurface using microtremor on the ground surface. *Quarterly Report of the Railway Technical Research Institute*, 30(1):25-33
- Okada Y (1985) Surface deformation due to shear and tensile faults in a half-space. *Bull Seismol Soc Am*, 75:1135-1154
- Pamuk, E., Özdağ, Ö.C., Özyalın, Ş. et al. (2017) Soil characterization of Tınaztepe region (İzmir/Turkey) using surface wave methods and nakamura (HVSR) technique. *Earthq. Eng. Eng. Vib.* 16, 447–458. <https://doi.org/10.1007/s11803-017-0392-y>

- Pamuk E, Gönenç T, Özdağ ÖC, Akgün M (2018) 3D Bedrock Structure of Bornova Plain and Its surroundings (İzmir/Western Turkey). *Pure and Applied Geophysics* 175:325–340. doi: 10.1007/s00024-017-1681-0
- Pamuk E, Özdağ ÖC, Akgün M (2018b) Soil characterization of Bornova Plain (Izmir, Turkey) and its surroundings using a combined survey of MASW and ReMi methods and Nakamura's (HVSR) technique. *Bulletin of Engineering Geology and the Environment* 78:3023–3035. doi: 10.1007/s10064-018-1293-7
- Pischiutta M, Akinci A, Tinti E, Herrero A (2020) Broad-band ground-motion simulation of 2016 Amatrice earthquake, Central Italy. *Geophysical Journal International* 224:1753–1779. doi: 10.1093/gji/ggaa412
- Pratt TL, Horton JW, Muñoz J, et al (2017) Amplification of Earthquake Ground Motions in Washington, DC, and Implications for Hazard Assessments in Central and Eastern North America. *Geophysical Research Letters* 44:12,150–160. doi: 10.1002/2017gl075517
- Soysal H, Sipahioglu S, Kolcak D, Altinok Y (1981) Türkiye ve Cevresinin Tarihsel deprem Katalogu. TUBITAK, Proje no. TBAG 341, Istanbul, 86 pp. **(in Turkish)**
- Sözbilir H, Sümer Ö, Uzel B, Ersoy Y, Erkül F, İnci U, Helvacı C. and Özkaymak Ç (2009) The Seismic geomorphology of the Sığacık Gulf (İzmir) earthquakes of October 17 to 20, 2005 and their relationships with the stress field of their Western Anatolian region. *Geological Bulletin of Turkey*, 52(2):217–238
- Stark PB, Parker RL (1995) Bounded-variable least-squares algorithm - An algorithm and implications. *Comput Stat*, 10(2):129-141
- Styron R, Pagani M (2020) The GEM Global Active Faults Database. *Earthquake Spectra* 36:160–180. doi: 10.1177/8755293020944182
- Tan O, Papadimitriou EE, Pabucçu Z, et al (2014) A detailed analysis of microseismicity in Samos and Kusadasi (Eastern Aegean Sea) areas. *Acta Geophysica* 62:1283–1309. doi: 10.2478/s11600-013-0194-1
- Taymaz T, Jackson J, Mckenzie D (1991) Active tectonics of the north and central Aegean Sea. *Geophysical Journal International* 106:433–490. doi: 10.1111/j.1365-246x.1991.tb03906.x
- Turkish Building Earthquake Code (TBEC) (2018). Disaster and Emergency Management Presidency, Ankara, Turkey **(in Turkish)**
- Turkish Seismic Code (TSC) (2007). Ministry of Public Works and Settlement, Ankara, Turkey **(in Turkish)**
- Turkish Statistical Institute (2021) Residential Building Permits. <https://data.tuik.gov.tr/>. Accessed 15 Jan 2021 **(in Turkish)**
- U.S. Geological Survey (2020) Earthquake Hazards Program, available at: <https://www.usgs.gov/natural-hazards/earthquake-hazards/earthquakes>, Accessed Jan 2021
- Uzel B, Sözbilir H, Özkaymak Ç, et al (2013) Structural evidence for strike-slip deformation in the İzmir–Balıkesir transfer zone and consequences for late Cenozoic evolution of western Anatolia (Turkey). *Journal of Geodynamics* 65:94–116. doi: 10.1016/j.jog.2012.06.009
- Vernant P, Reilinger R, McClusky S (2014) Geodetic evidence for low coupling on the Hellenic subduction plate interface. *Earth and Planetary Science Letters* 385:122–129. doi: 10.1016/j.epsl.2013.10.018

Zandieh A, Pezeshk S (2011) A Study of Horizontal-to-Vertical Component Spectral Ratio in the New Madrid Seismic Zone. *Bulletin of the Seismological Society of America* 101:287–296. doi: 10.1785/0120100120

Zhu L, Mitchell BJ, Akyol N, et al (2006) Crustal thickness variations in the Aegean region and implications for the extension of continental crust. *Journal of Geophysical Research*. doi: 10.1029/2005jb003770

## Tables

**Table 1.** Strong motion stations which recorded the mainshocks of the 30 October 2020 Samos (eastern Aegean Sea) earthquake.

<i>Station Code</i>	<i>LAT</i>	<i>LON</i>	<i>Distance</i> <i>R<sub>epi</sub></i> <i>(km)</i>	<i>PGA-EW</i> <i>(g)</i>	<i>PGA-NS</i> <i>(g)</i>	<i>PGA-UD</i> <i>(g)</i>	<i>PGV-NS</i> <i>(cm/s)</i>	<i>PGV-EW</i> <i>(cm/s)</i>	<i>PGV-UD</i> <i>(cm/s)</i>	<i>V<sub>S30</sub></i> <i>(m/s)</i>	<i>EC8</i>
SMG1	37.753	26.978	21.5	0.232	0.162	0.137	24.1	18.8	10.6	-	-
GMLD	38.076	26.874	22.6	0.189	0.269	0.128	21.78	17.27	6.43	-	B
3536	38.196	26.838	34.69	0.081	0.051	0.032	5.31	8.71	3.56	1141	A
0905	37.859	27.265	43.05	0.147	0.183	0.081	7.83	8.87	4.54	369	B
3523	38.328	26.770	48.85	0.065	0.082	0.038	5.71	4.97	4.10	414	B
3533	38.257	27.130	51.37	0.047	0.075	0.038	5.51	5.93	3.37	415	B
3516	38.370	26.890	54.48	0.049	0.048	0.033	4.82	3.63	2.43	460	B
0911	37.762	27.390	55.83	0.068	0.049	0.048	4.31	4.52	2.76	307	C
3538	38.318	27.123	56.63	0.078	0.087	0.040	5.47	6.08	2.66	-	-
3528	38.303	26.372	58.22	0.152	0.120	0.078	7.54	8.32	3.62	532	B
3506	38.394	27.082	62.24	0.042	0.045	0.024	3.38	3.15	2.07	771	B
0920	37.560	27.374	64.04	0.031	0.026	0.022	3.00	2.69	1.99	894	A
3517	38.375	27.193	65.29	0.037	0.041	0.020	3.95	3.48	2.10	695	B
3512	38.400	27.151	65.71	0.058	0.059	0.029	3.31	3.89	1.58	468	B
3518	38.431	27.143	68.31	0.093	0.108	0.032	1131	10.64	8.32	298	C
3519	38.452	27.111	69.16	0.112	0.153	0.035	22.52	14.48	4.32	131	D
3521	38.467	27.076	69.50	0.096	0.113	0.041	16.17	12.29	3.86	145	D
3522	38.435	27.198	71.14	0.065	0.075	0.025	9.92	14.79	3.72	249	C
0918	37.369	27.264	71.84	0.032	0.039	0.021	5.99	4.97	4.09	630	B
3513	38.458	27.167	71.94	0.097	0.108	0.045	17.08	14.42	4.74	196	C
3511	38.421	27.256	72.58	0.042	0.030	0.019	3.96	5.96	1.87	827	A
3514	38.476	27.158	73.32	0.057	0.040	0.026	4.21	6.41	1.93	836	A
3524	38.496	27.107	73.51	0.070	0.066	0.030	4.70	5.90	1.92	459	B
3520	38.478	27.211	75.72	0.060	0.037	0.020	4.65	8.36	2.68	875	A
3526	38.578	26.979	78.63	0.083	0.090	0.030	10.82	10.43	3.41	205	C
3534	38.662	26.758	85.96	0.094	0.075	0.039	5.06	4.91	2.63	328	C
3539	38.1022	27.721	86.26	0.028	0.038	0.023	2.68	1.93	1.75	-	-
3527	38.639	26.512	86.50	0.058	0.082	0.048	8.84	7.02	6.06	207	C
4501	38.612	27.381	96.26	0.041	0.036	0.025	7.05	6.79	3.53	340	-
3503	39.073	26.888	131.99	0.046	0.057	0.017	6.68	5.54	1.98	193	C

3537	39.109	27.170	139.87	0.008	0.008	0.007	1.89	1.55	1.58	608	B
3508	39.088	27.374	143.07	0.017	0.015	0.008	2.08	1.69	1.01	558	B

**Table 2.** Model parameters for the finite-fault simulation of the 30 October 2020 Samos (eastern Aegean Sea) earthquake.

Parameter	Value	Reference
Moment Magnitude	7.0	EMSC-USGS - SLU - INGV
Hypocentral Depth	16 km	AFAD
Fault plane orientation	285° - 38°	This study
Fault Length and width	50 x 25 km	This study
Stress Drop	80 bars	This study (best-fit estimate)
Crustal Density	2800 kg m <sup>-3</sup>	Çubuk-Sabuncu et al. (2017)
Crustal shear wave velocity, $V_s$	3.5 km s <sup>-1</sup>	Çubuk-Sabuncu et al. (2017)
Rupture Velocity	0.8 x $V_s$	-
Pulsing Percentage	50%	-
Slip model subfaults	2.5 x 2.5 km	This study
Geometrical Spreading Coe.	$r^{-1.0}$ $r < 40$ km $r^{-0.8}$ $40 < r < 80$ km $r^{-0.7}$ $r > 100$ km	Akinci et al. (2013)
Anelastic Attenuation	$180f^{0.55}$	Akinci et al. (2013)
Kappa parameters, $\kappa$	0.045 s and 0.055 s	Akinci et al. (2013)
Site amplifications	class A ( $V_{s30}$ 1140 m/s) class B ( $V_{s30}$ 620 m/s) class C and D ( $V_{s30}$ 255 m/s)	Pischiutta et al. (2020) Boore and Joyner (1997) Boore and Joyner (1997)

## Figures

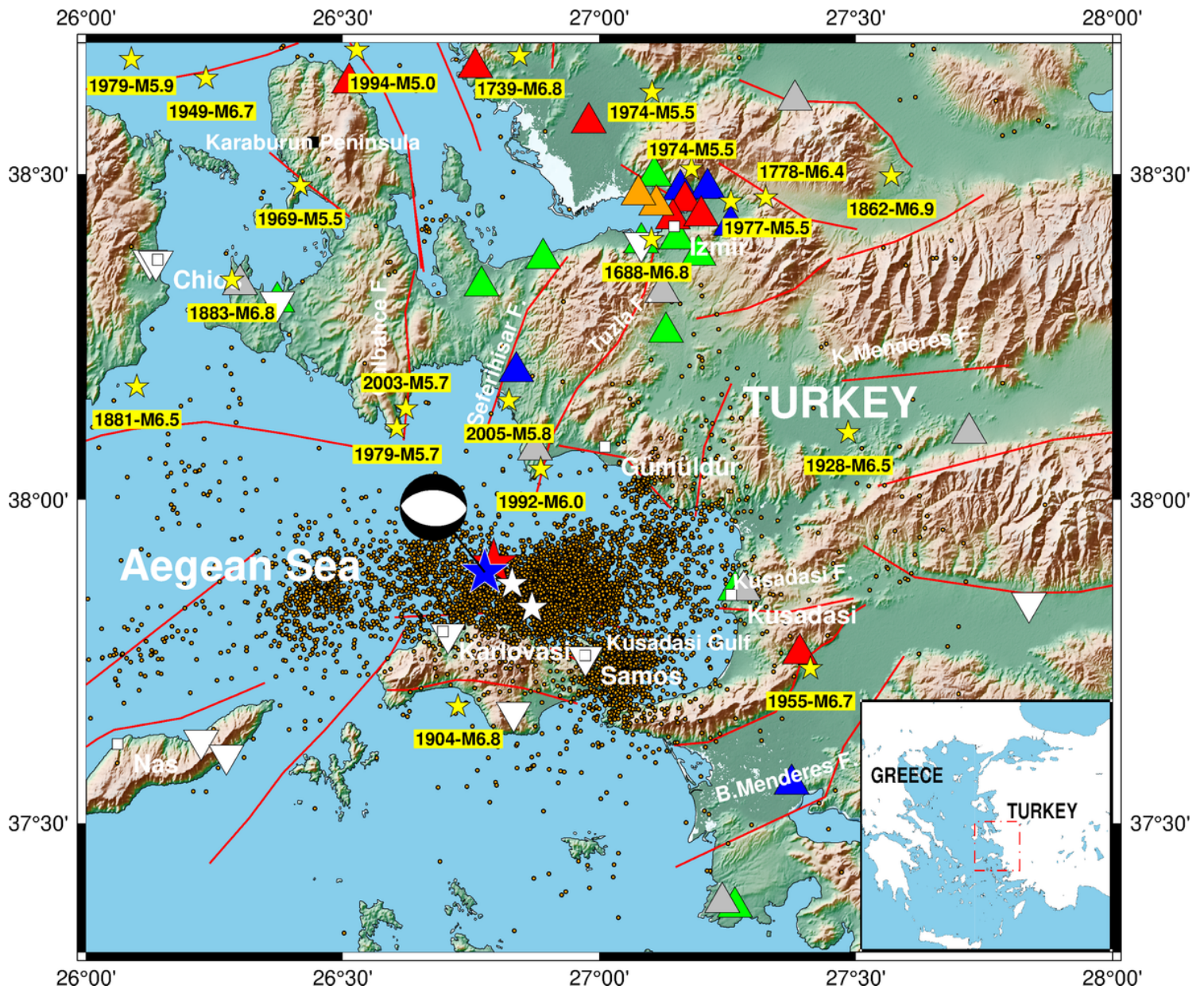


**Figure 1**

Seismotectonic setting of the study area. The solid lines represent the main fault segments from the GEM fault database (Styron & Paganì 2020). Seismicity: the orange dots are the aftershocks (quick solutions) recorded between 30 October 2020 and 13 January 2021 (available at <http://www.koeri.boun.edu.tr/sismo/2/latest-earthquakes/map/>); the blue and red stars represent the locations of the mainshock provided by AFAD and KOERI, respectively, with the relative moment tensor solution (red beach-ball, U.S. Geological Survey 2020); the white stars are the location of the major ( $M \geq 5$ ) events of the seismic sequence; the yellow stars depict the epicenter of the major earthquakes of the instrumental era (from Makropoulos et al. 2012; Ambraseys 2009; Duman et al. 2018). The inverted white triangles represent the geodetic stations, while the coloured triangles indicate seismic station locations. The red dashed box in the inset shows the area of the main figure.

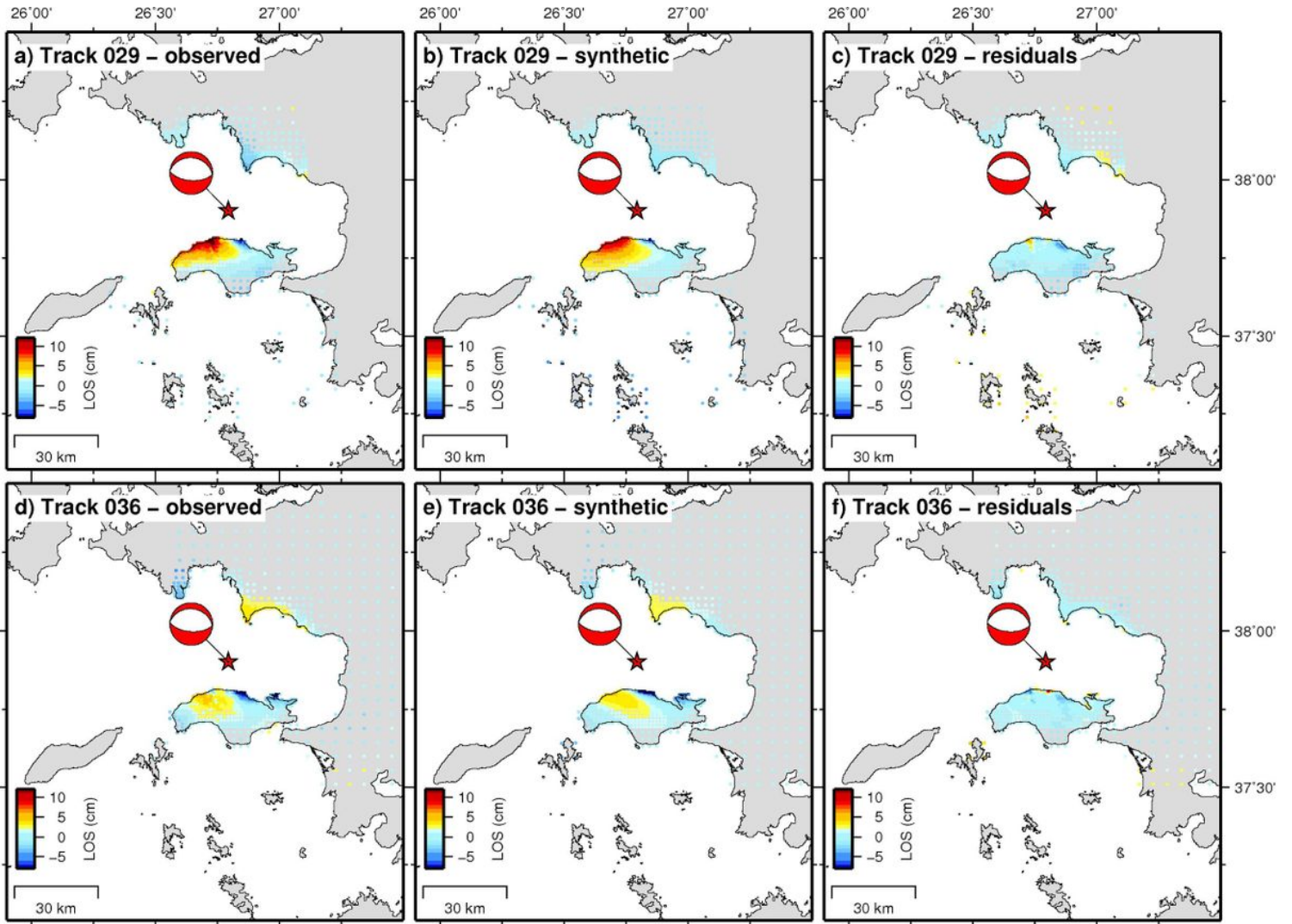


**Figure 2**

Observed, modelled, and residual sampled points from the InSAR Sentinel-1 ascending (panels a, b, and c) and descending (panels d, e and f) unwrapped interferograms, respectively. The red star represents the mainshock epicentre provided by KOERI.

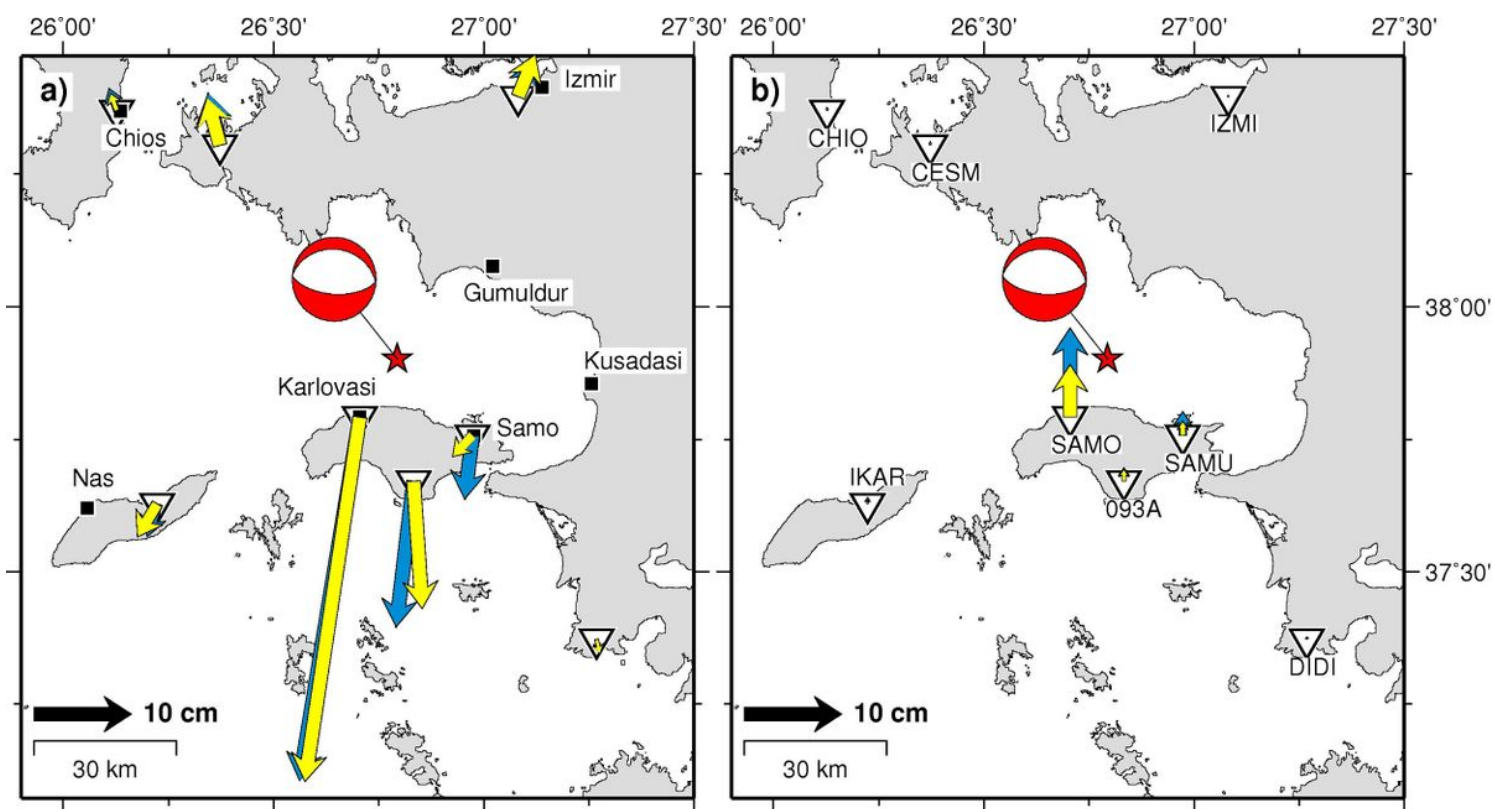


**Figure 3**

Observed (blue) and modeled (yellow) GPS displacements: (a) horizontal, and (b) vertical displacements, respectively. The red star represents the mainshock epicenter (KOERI).

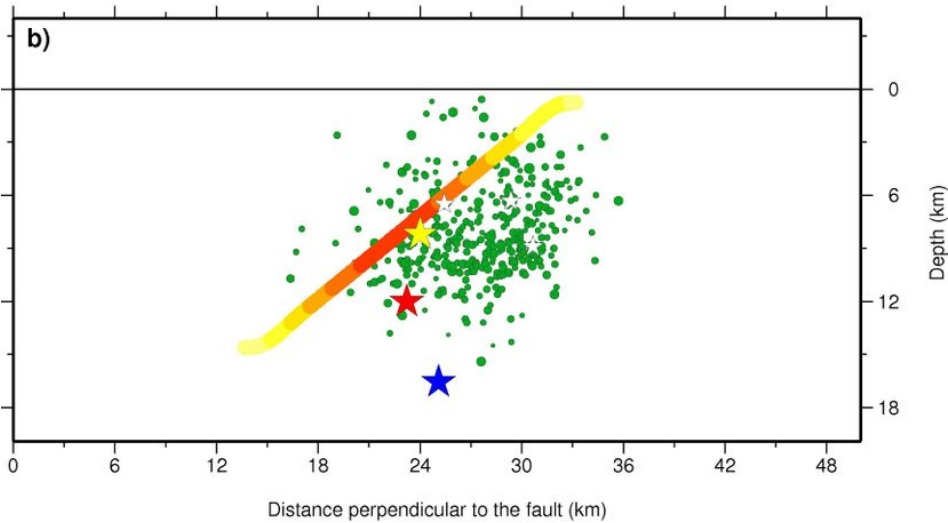
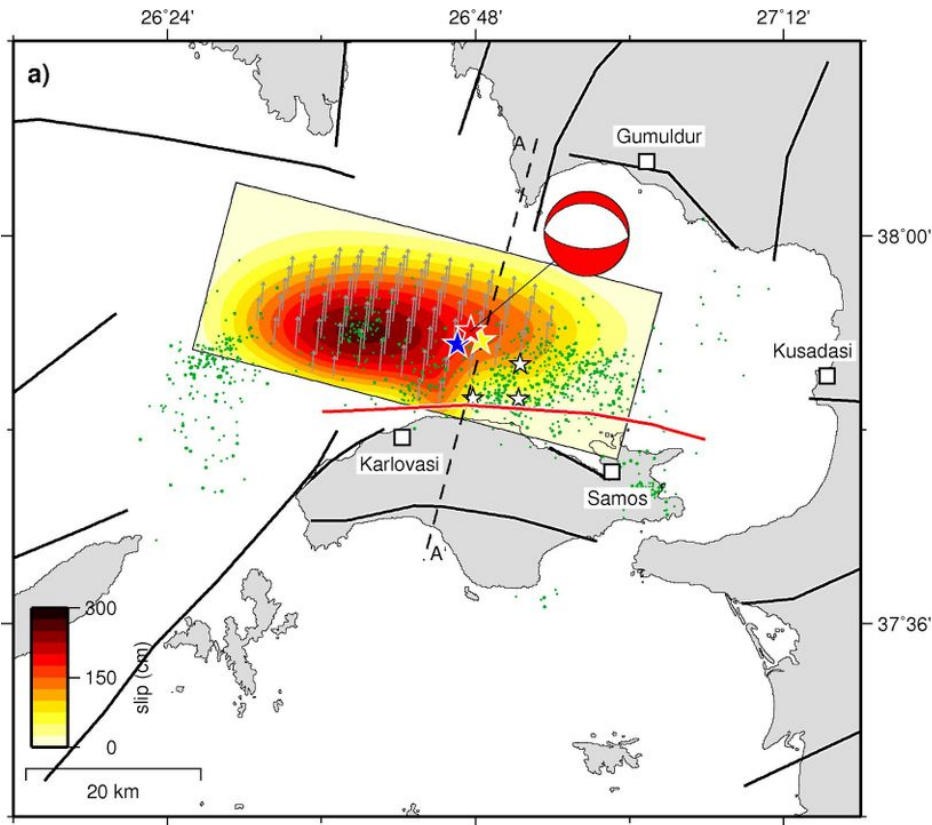


**Figure 4**

(a) Coseismic slip distribution on the preferred fault model. The blue and red stars represent the AFAD and KOERI locations of the mainshock, respectively, while the yellow star is the relocated solution (Cetin et al. 2020); the white stars are the major aftershocks with  $M \geq 4.5$ . Green circles are relocated aftershocks between 30 October 2020 and 30 November 2020 (Cetin et al. 2020). The red beach ball indicates the mechanisms of the mainshock from the USGS solution. Grey arrows indicate slip directions on fault patches. Other symbols as in Figure 1. (b) Cross section drawn perpendicular to the strike of the fault, showing the slip distribution as a function of depth and the seismic events locations (symbols as in the top panel).

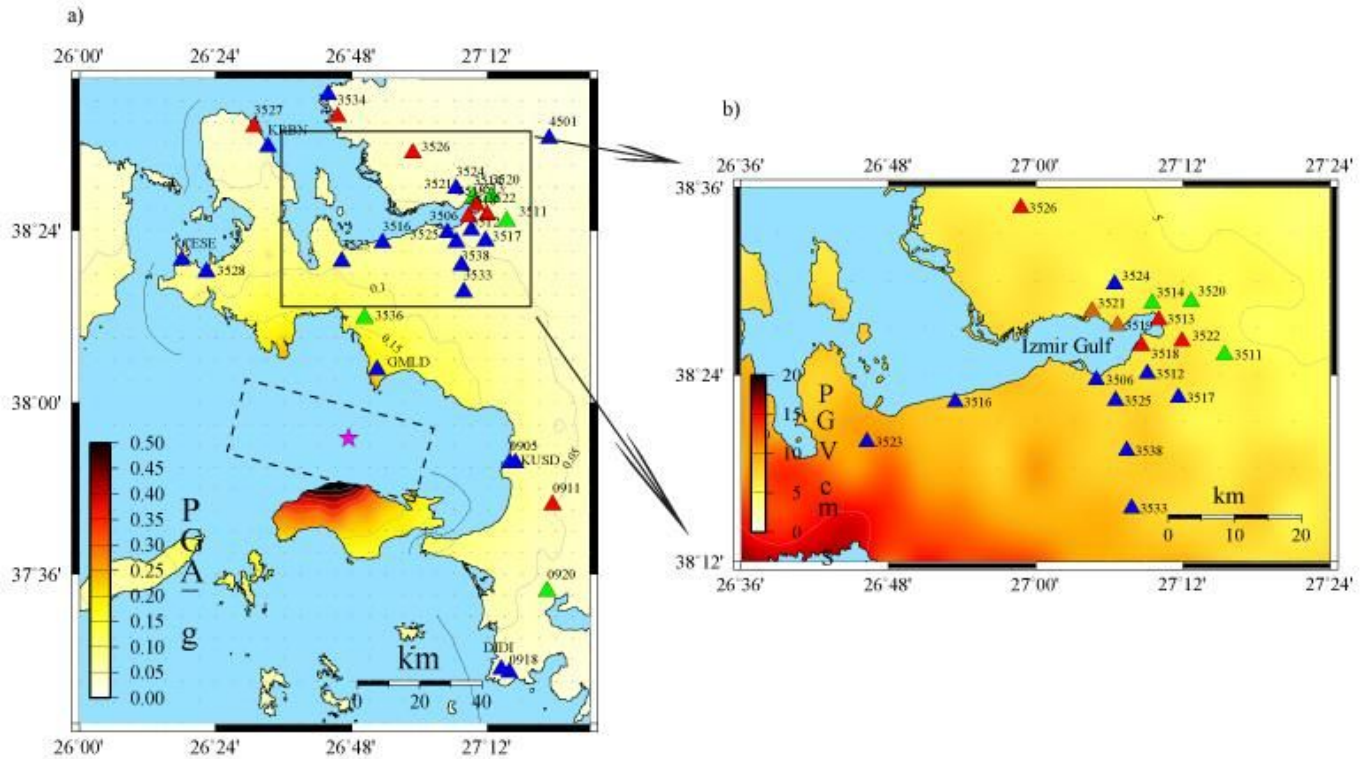


**Figure 5**

Spatial distributions of stochastic ground motion in terms of (a) PGA (g) over the study area and (b) PGV (m/s) variation in Izmir and surrounding areas obtained using the parameters given in Table 2 at the engineering rock site,  $V_{s30} = 760$  m/s over the 1055 virtual stations located at 5 km grid spacing. Locations of strong motion stations are given by colored triangles indicating the type of the site classifications associated with each station. Rectangular dashed box presents the fault surface projection. Star indicates the epicentral location of the mainshock as provided by AFAD.

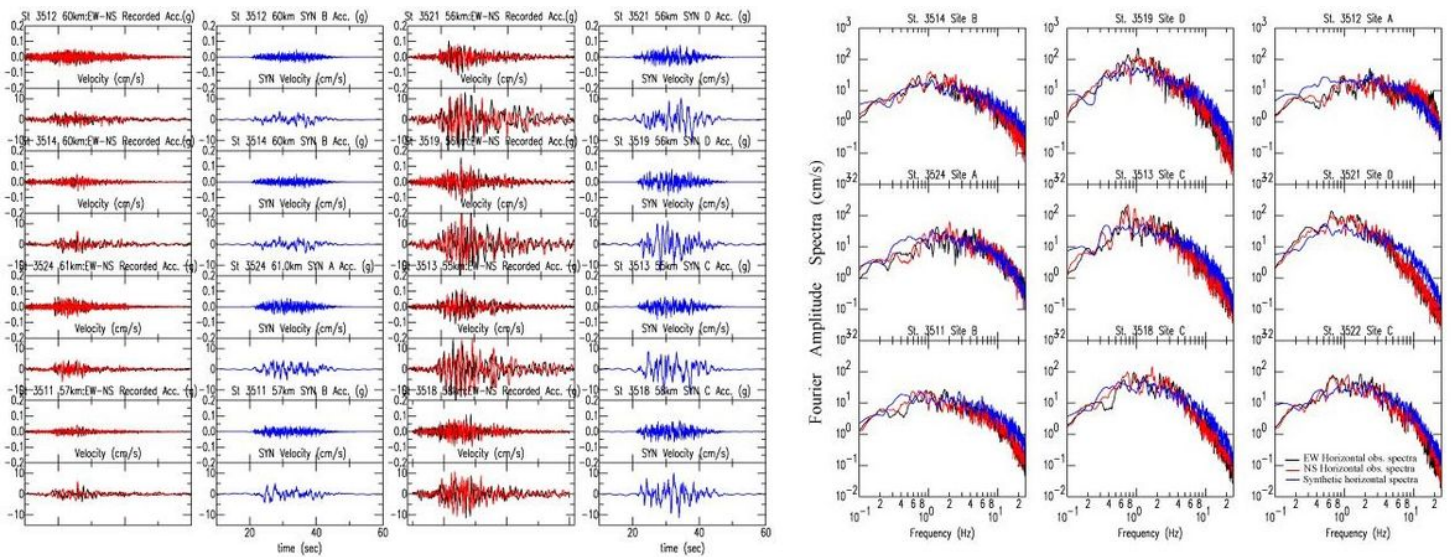


**Figure 6**

Comparisons between (a) observed and simulated (SYN) acceleration and velocity time histories and (b) Fourier Amplitude spectra at selected stations in the Izmir metropolitan area. Recorded horizontal ground motion data are indicated with black and red for NS and EW components, respectively, while synthetics are presented in blue.

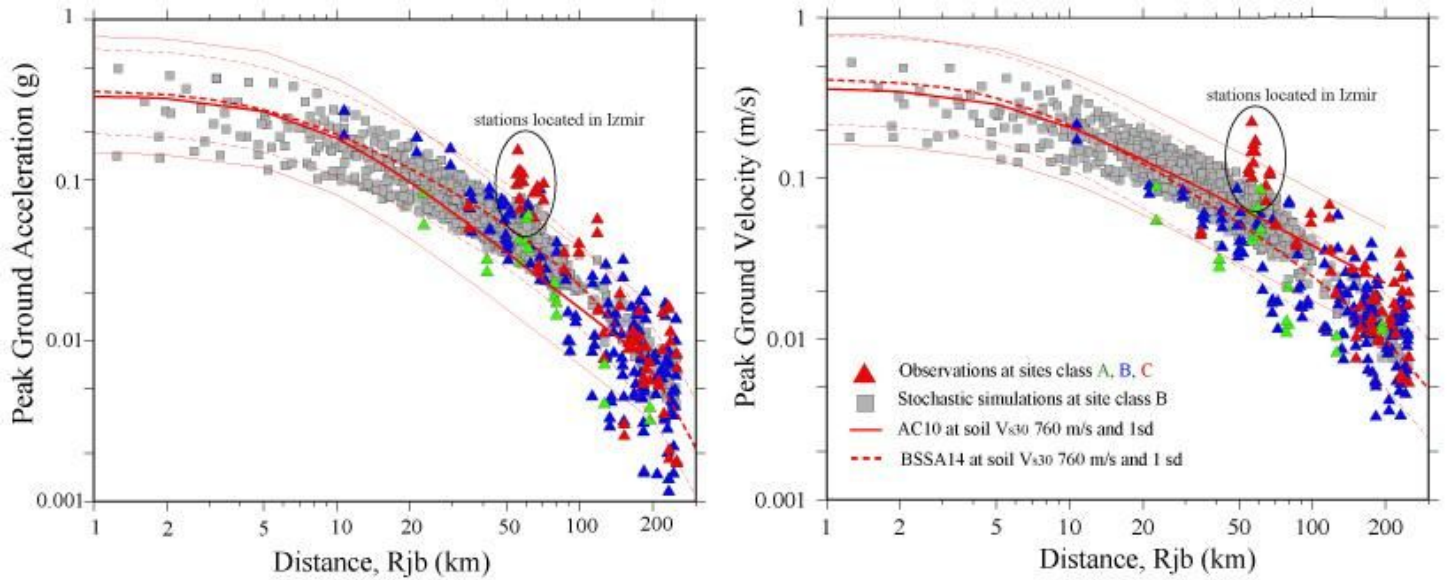


**Figure 7**

Comparison of observed horizontal (a) peak ground acceleration (PGA g) and (b) peak ground velocity (PGV m/s) values of Samos earthquake MW 7.0 at rock (green), stiff (blue) and soft (red) soil site against the simulated ground motion parameters calculated at 1055 virtual stations and the ground motion prediction models of BSSA14 (Boore et al. 2014) and AC10 (Akkar and Cagnan 2010). PGA and PGV values recorded by the stations located in the Izmir metropolitan area are grouped and highlighted in the same figure.

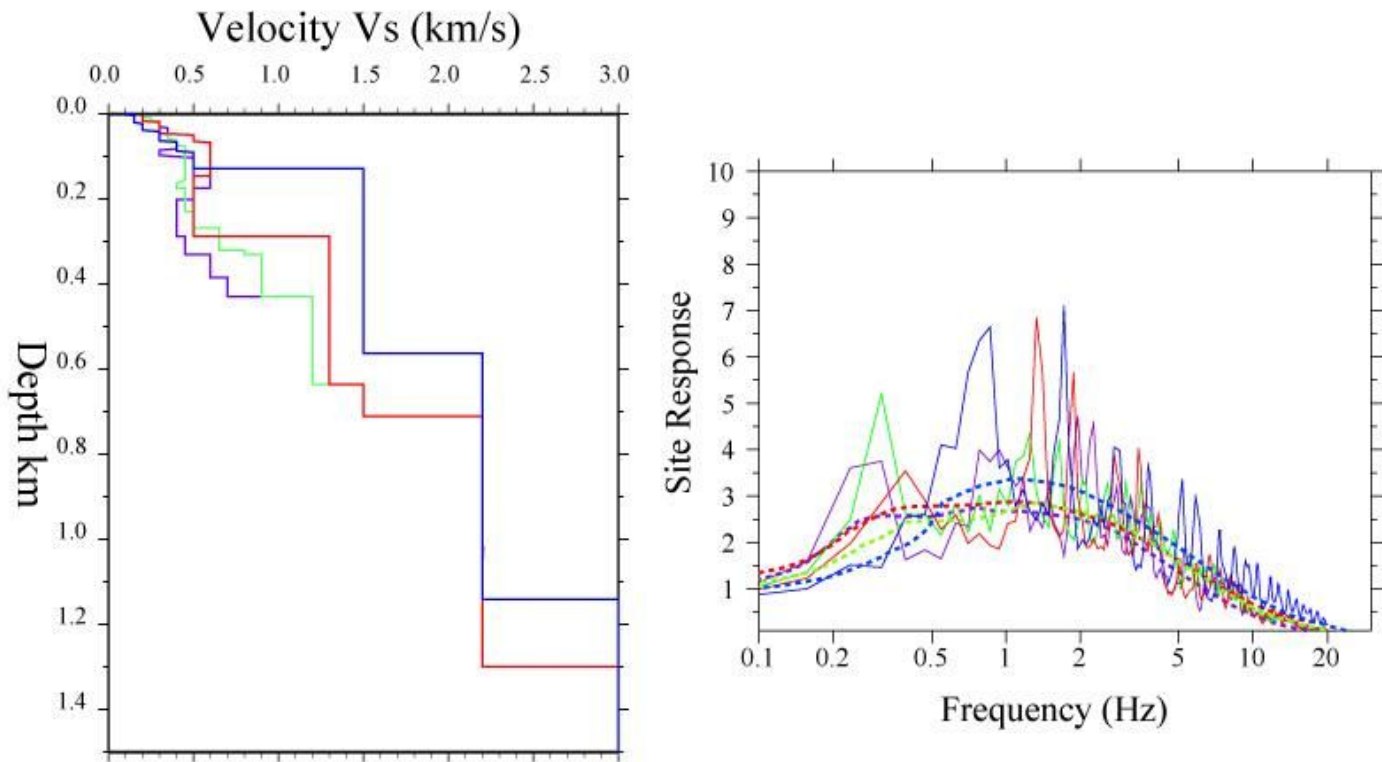


**Figure 8**

(a) The velocity profiles S2 (violet), S3 (green), S4 (blue) and S5 (red) adopted from the Pamuk et al. (2018) and used for site amplifications in the Izmir Bay area. (b) Site responses are calculated using four velocity profiles through the PPM (continues curves) and QWL (dashed curves) method, for this model  $\kappa=0.05$  s.

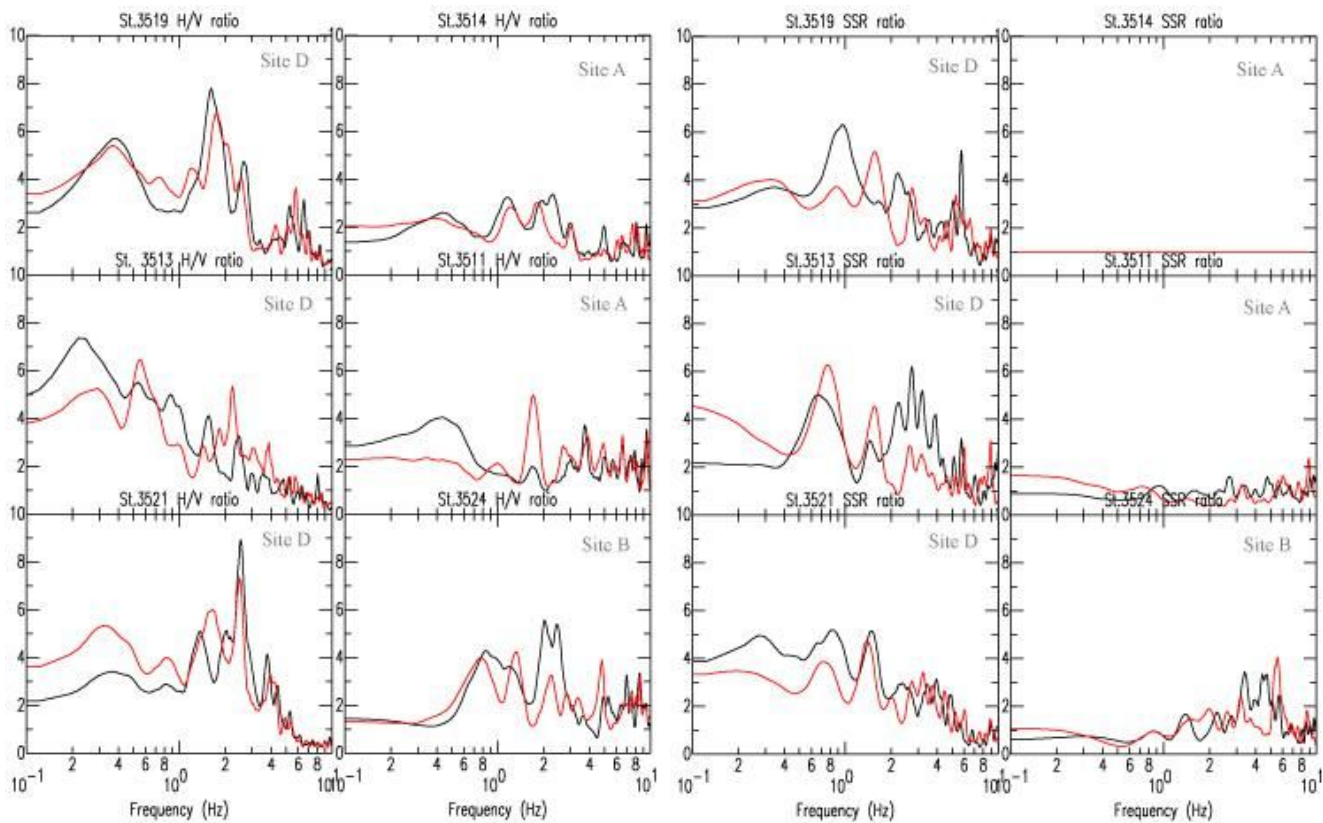


**Figure 9**

Site amplification functions together with well-defined resonance peaks from a) the H/V spectral ratio and b) the SSR Spectral ratio of S waves at six recording sites selected from those deployed in the Izmir metropolitan area (3519, 3513 and 3521 located on the soft soil while 3514, 3511 and 3524 on the stiff and rock site). Ratios are shown for the two components of the mainshock, MW 7.0 (black and red curves in each frame).

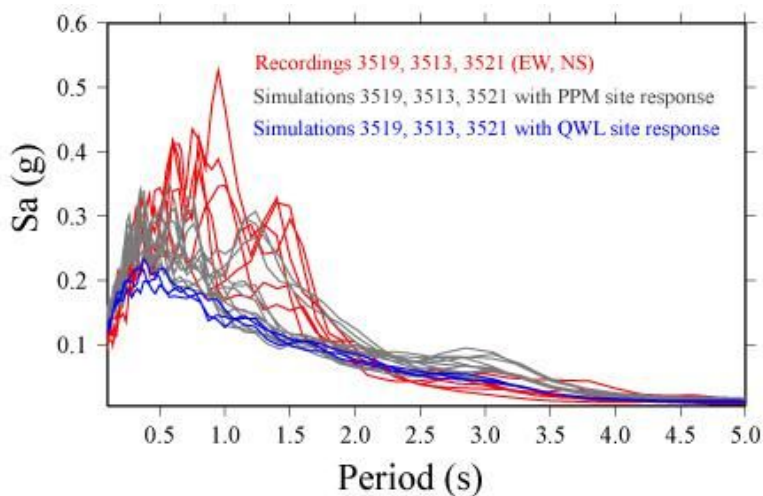


**Figure 10**

The spectral acceleration from the recorded on the horizontal components (red) and simulated seismograms using the site amplifications derived from the PPM (grey) and QWL (blue) approximations at three sites 3519, 3513 and 3521 located in the Izmir Bay area.

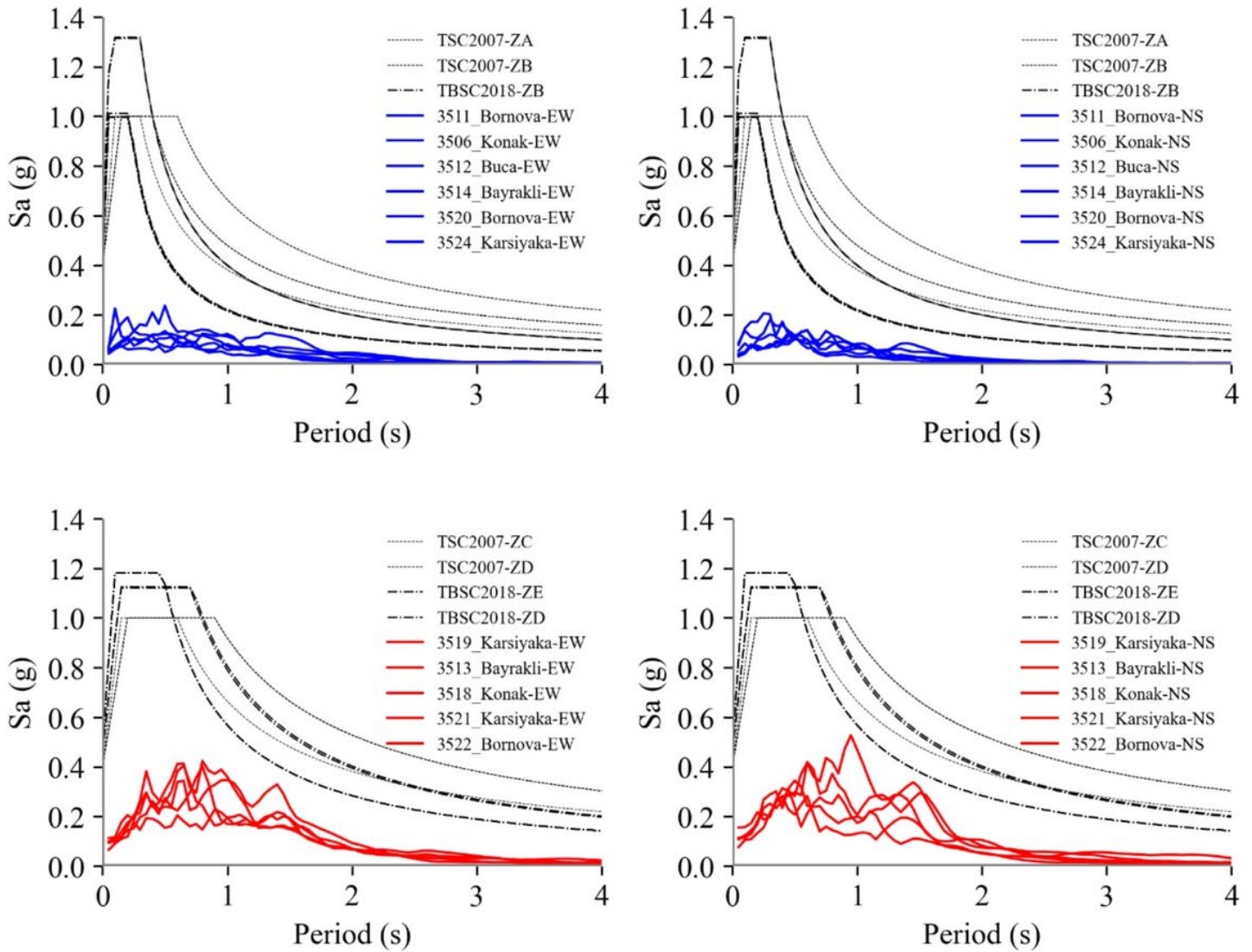


**Figure 11**

Comparison of the response spectrum of twelve strong motion records with Seismic Design Codes of 2007 and 2018 spectrum grouped in hard (blue) and soft (red) soils at top and bottom rows, respectively, also EW and NS components at each row, respectively.

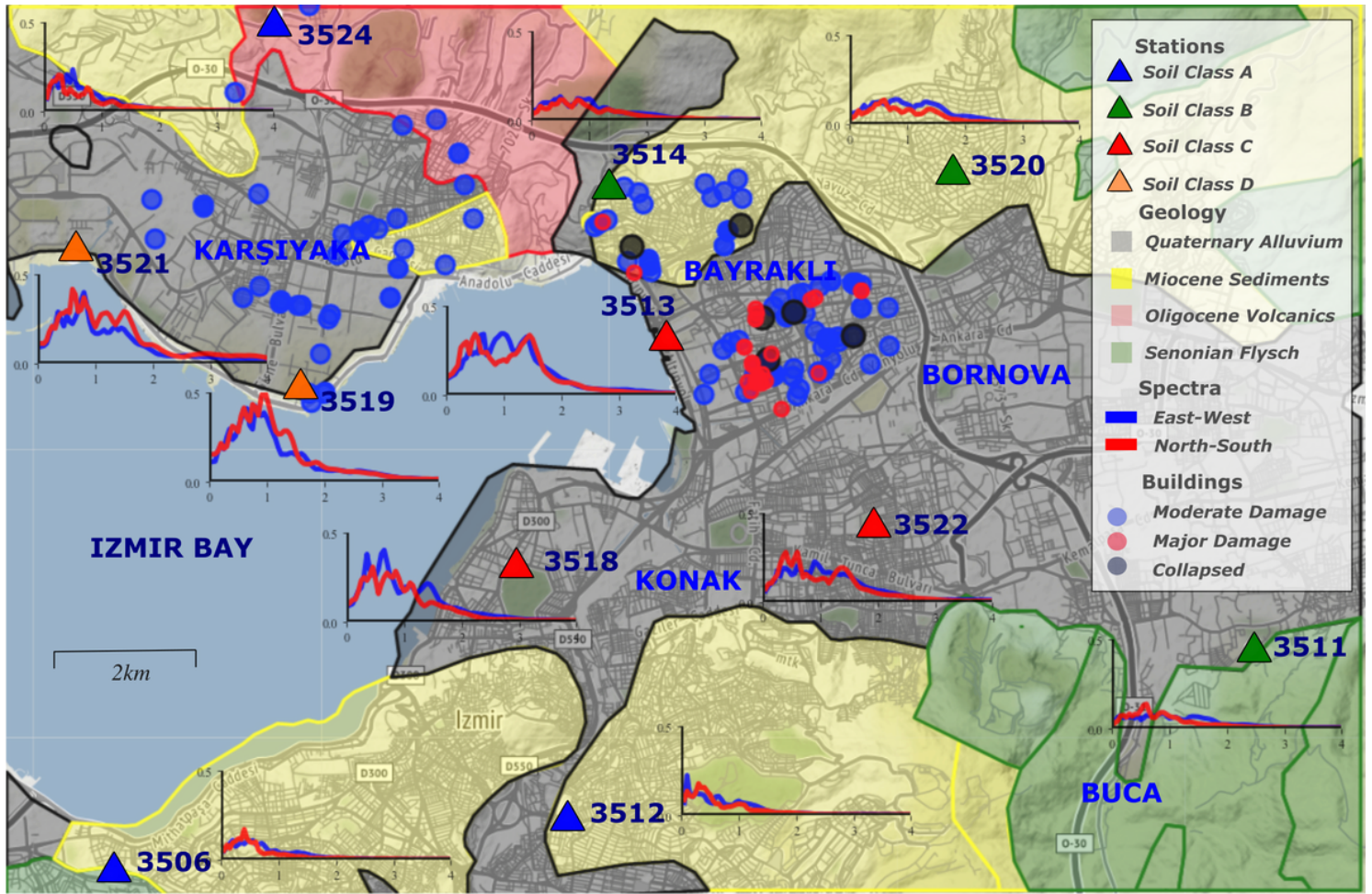


**Figure 12**

Distribution of AFAD ground motion stations (AFAD 2020) and response spectrum curves obtained in the station, building damage (Ministry of Environment and Urbanization), Geology of Izmir Metropolitan Area (General Directorate of Mineral Research and Exploration).

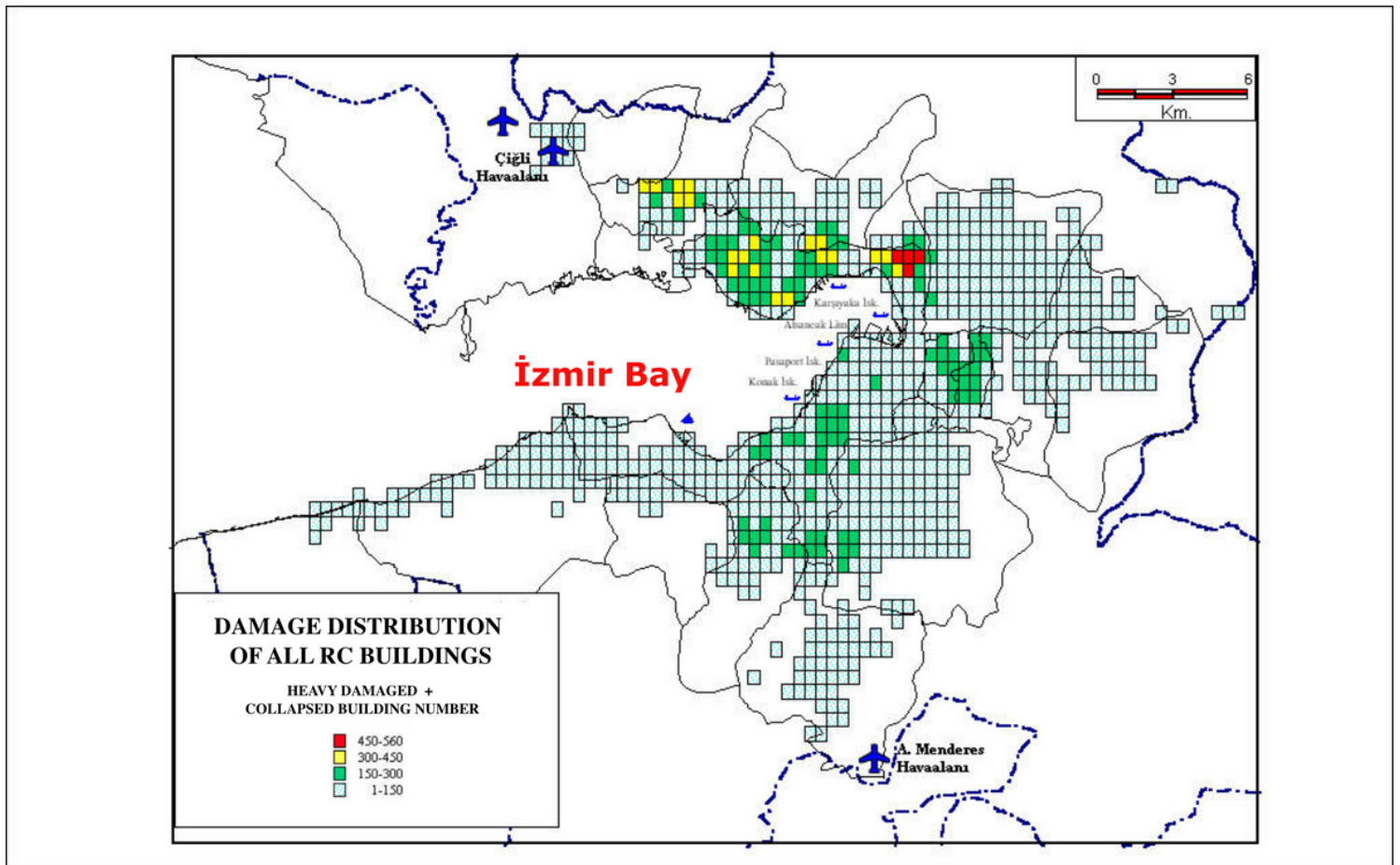


**Figure 13**

Predicted distribution of heavy damage and collapse potential buildings in İzmir Metropolitan Area (English translation of the map from İzmir Earthquake Master Plan, MMI 2000).

## Supplementary Files

This is a list of supplementary files associated with this preprint. Click to download.

- [20210121AkincietaI BEE2021SupplementaryMat.docx](#)